

# Implementation and application of Ensemble Optimal Interpolation on an operational chemistry weather model for improving PM<sub>2.5</sub> and visibility predictions

Siting Li<sup>1</sup>, Ping Wang<sup>1</sup>, Hong Wang<sup>1</sup>, Yue Peng<sup>1</sup>, Zhaodong Liu<sup>1</sup>, Wenjie Zhang<sup>1</sup>, Hongli Liu<sup>1</sup>, Yaqiang Wang<sup>1</sup>, Huizheng Che<sup>1</sup>, Xiaoye Zhang<sup>1</sup>

<sup>1</sup>State Key Laboratory of Severe Weather & Key Laboratory of Atmospheric Chemistry of CMA, Chinese Academy of Meteorological Sciences, Beijing, China

*Correspondence to:* Ping Wang (wangp@cma.gov.cn); Hong Wang (wangh@cma.gov.cn)

**Abstract.** The data assimilation technique is one of the important ways to reduce the uncertainty of atmospheric chemistry model input and improve the model forecast accuracy. In this paper, an ensemble optimal interpolation assimilation (EnOI) system for a regional online chemical weather numerical forecasting system (GRAPES\_Meso5.1/CUACE) is developed for operational use and efficient updating of the initial fields of chemical components. A heavy haze episode in eastern China was selected, and the key factors affecting the EnOI, such as localization length-scale, ensemble size, and assimilation moment, were calibrated by sensitivity experiments. The impacts of assimilating ground-based PM<sub>2.5</sub> observations on the model chemical initial field and PM<sub>2.5</sub>, visibility forecasts were investigated. The results show that assimilation of PM<sub>2.5</sub> ~~significantly~~ reduces the uncertainty of the initial PM<sub>2.5</sub> field ~~considerably. The mean error and root mean square error (RMSE) of initial PM<sub>2.5</sub> for mainland China have all decreased by more than 75%, and the correlation coefficient could be improved to more than 0.95. Even greater improvements appear in North China. Using only 50% observations to do the assimilation, the root mean square error (RMSE) of initial PM<sub>2.5</sub> for independent verification sites in mainland China decreases from 73.7 to 46.4  $\mu\text{g m}^{-3}$ , and the correlation coefficient increases from 0.58 to 0.84. An even larger improvement appears in North China.~~ For the forecast fields, assimilation of PM<sub>2.5</sub> improves PM<sub>2.5</sub> and visibility forecasts throughout the ~~lead~~-time window of 24 h. The PM<sub>2.5</sub> RMSE can be reduced by 10%-21% within 24 h, ~~but and~~ the assimilation effect is most ~~obvious-remarkable~~ in the first 12 h. ~~The assimilation moment chosen at 1200 UTC is more effective than that at 0000 UTC for improving the forecast, because the discrepancy between simulation and observation at 1200 UTC is larger than that at 0000UTC, indicating the assimilation efficiency will be higher when the bias of the model is higher. Within the same assimilation time, the assimilation efficiency varies with the discrepancy between model forecasts and observations at the moment of assimilation, and the larger the deviation, the higher the efficiency. Assimilation of PM<sub>2.5</sub> also improves visibility forecast accuracy significantly. The assimilation of PM<sub>2.5</sub> further contributes improvement of visibility forecast.~~ When the PM<sub>2.5</sub> increment is negative, it corresponds to an increase in visibility, and when the PM<sub>2.5</sub> analysis increment is positive, visibility decreases. It is worth noting that the improvement of visibility forecasting by assimilating PM<sub>2.5</sub> is more obvious in the light pollution period than in the heavy pollution period, since visibility is much more affected by humidity during the heavy pollution period

accompanied by low or extreme low visibility. To get further visibility improvement, especially for extreme low visibility during severe haze pollution, not only PM<sub>2.5</sub> but also relative humidity should be simultaneously assimilated as well. ~~The results of this study shows that the EnOI may provide a practical and cost-effective alternative to the EnKF for the applications where computational cost is a main limiting factor, especially for real-time operational forecast.~~

## 1 Introduction

Air pollution is an intractable problem that all developing countries with high population in the world are facing at present. ~~The rapid development of industrialization and urbanization has led to different degrees of air pollution in many countries and regions (Perez et al., 2020; Xiao et al., 2020; Sahu and Kota, 2017). The energy-intensive and coal-fired economy in China has led to a dramatic deterioration in air quality over the past three decades (Piovani, 2017).~~ PM<sub>2.5</sub> plays an important role in air pollution, and its concentration will directly affect air quality. From the health perspective, long-term exposure to high concentrations of PM<sub>2.5</sub> has adverse effects on the human body, including the respiratory system, cardiovascular disease and other chronic diseases (Ghorani-Azam et al., 2016). ~~From the meteorological perspective, aerosol particles can effectively absorb and scatter solar radiation, change the intensity and direction of sunlight, reduce atmospheric horizontal visibility (Liu et al., 2019; Yadav et al., 2022; Ting et al., 2022), leading to low visibility events occur frequently during the haze period episodes which are characterized by significant growth in the concentration of aerosol particles and sharp reduction of visibility. Aerosol particles can effectively absorb and scatter solar radiation, changing the intensity and direction of sunlight, resulting in reduced atmospheric horizontal visibility (Liu et al., 2019; Yadav et al., 2022; Ting et al., 2022), which will affect people's daily travel and traffic safety, etc.~~

Accurate PM<sub>2.5</sub> and visibility forecasts are critical for human health, air quality assessment and public transportation safety issues (Zhang et al., 2013). Chemistry Transport Model (CTM) or Coupled chemistry meteorology models (CCMM) are a key important tools for PM<sub>2.5</sub> and visibility forecasting, and is pivotal in air quality and atmospheric chemistry research. However, various uncertainties exist in the simulation of atmospheric components in CTM or CCMM, especially for aerosols (Lee et al., 2016). The complexity of atmospheric pollution formation mechanisms and model structure, the uncertainty of chemical initial conditions (ICs) and the lag in emission inventories lead to a deviation of air quality forecast results from observed comparisons, ~~which can reach 30-50% under heavy pollution conditions (Zheng et al., 2015). The forecast accuracy of air quality forecasting still needs to be improved (Wang et al., 2016; Peng et al., 2021b).~~

Data assimilation (DA) is one of the most effective ways to improve model predictions. ~~It combines observational information with numerical models to provide an estimate of the state of the system which is widely used in atmospheric, oceanic, and land surface surveys. DA were earliest applied to numerical weather prediction (Navon, 2009). There are many DA methods for example, Polynomial Interpolation (Panofsky, 1949; Gilchrist and Cressman, 1954), the methods of successive corrections (Bergthórsson and Döös, 1955), and the Kalman Filter (KF) (Kalman, 1960), the optimal interpolation (OI) (Gandin,~~

1963), the variational assimilation methods (e.g., the three-dimensional variational assimilation (3D-VAR), the four-dimensional variational assimilation (4D-Var)) (Talagrand and Courtier, 1987; Derber, 1989), Ensemble Kalman filter method (EnKF) (Evensen, 1994), Ensemble Optimal Interpolation (EnOI) (Oke et al., 2002; Evensen, 2003), etc. The use of data assimilation in atmospheric chemistry models to improve air quality forecasting is more recent. For example, by assimilating aerosol observations with OI (Zheng et al., 2018; Tombette et al., 2009; Carnevale et al., 2021; Tang et al., 2015; Mauricio Agudelo et al., 2015); 3D-Var (Fu and Zhu, 2011; Feng et al., 2018; Wang et al., 2020; Li et al., 2013; Liu et al., 2011; Ye et al., 2021); 4D-Var (Cao et al., 2022; Wang et al., 2021; Liu et al., 2021; Skachko et al., 2016; Zhang et al., 2011); EnKF (Lin et al., 2007; Tang et al., 2011; Pagowski and Grell, 2012; Tang et al., 2016; Lopez Restrepo et al., 2020; Park et al., 2022); EnOI (Wang et al., 2016); Four-dimensional ensemble Kalman filter (4D-EnKF) (Cheng et al., 2019); Four-Dimensional Local Ensemble Transform Kalman Filter (4D-LETKF) (Dai et al., 2019). Weather prediction had relied on data assimilation for many decades (Kalnay, 2003; Navon 2009). In comparison, the use of data assimilation in atmospheric chemistry models to improve air quality forecasting is more recent, but important advances have been made. Tombette et al. (2009) presented an experiment on PM<sub>10</sub> data assimilation using OI method to improve PM<sub>10</sub> forecasting. Tang et al. (2015) used the same DA method to assimilate ozone/ PM<sub>2.5</sub> and MODIS aerosol optical depth data into the Community Multi-scale Air Quality model to improve the ozone and total aerosol concentration for the CMAQ simulation over the contiguous United States. Liu et al. (2011) assimilated AOD from Terra and Aqua satellites using the GSI 3D-Var assimilation system, showing that AOD data assimilation system can serve as a tool to improve simulations of dust storms. Li et al. (2013) and Feng et al. (2018) assimilated ground-based observations of PM<sub>2.5</sub> using 3D-Var to improve PM<sub>2.5</sub> forecasting. 4D-Var has been successfully implemented on CTMs and has improved the PM<sub>2.5</sub> forecasting capability. Zhang et al. (2016) constructed a GEOS-Chem adjoint model suitable for PM<sub>2.5</sub> pollution diffusion based on 4DVAR algorithm, which was verified by the monitoring data of APEC in Beijing in 2014. Zhang et al. (2021) built a PM<sub>2.5</sub> data assimilation system based on the 4DVar algorithm and the WRF-CMAQ model, which can assimilate synchronous observations simultaneously to improve aerosol prediction accuracy. Wang et al. (2021) established a 4D-VAR assimilation system based on GRAPES\_CUACE to optimize black carbon (BC) daily emissions in northern China on 4 July 2016. EnKF also plays a significant role in improving the accuracy of atmospheric chemistry model forecasts. Lin et al. (2007) developed a EnKF system for a regional dust transport model. Tang et al. (2016) investigated a cross-variable ozone DA method based on an EnKF, for improving ozone forecasts over Beijing and surrounding areas. Park et al. (2022) developed a DA system for the CTM using the EnKF technique, where PM<sub>2.5</sub> observations from ground stations are assimilated to ICs every 6 hours to improve PM<sub>2.5</sub> forecasting in the Korean region. Peng et al. (2017) used EnKF to optimize ICs and emission input, resulting in significant improvements in PM<sub>2.5</sub> forecast. Overviews of these achievements were provided in several literatures (Bocquet et al., 2015; Benedetti et al., 2018; Zhu et al., 2018; Sokhi et al., 2022). Although the previous studies have reported DA method using ground-based or satellite-retrieved observation led to improvement of atmospheric composition prediction, each of these DA methods has its own limitation. In OI and 3D-Var, the background error covariance (BEC) matrix is estimated at once and the prediction error is statistically stationary. 4D-Var and

EnKF are advanced data assimilation methods that provide the evolution of the forecast error covariance, but when they are employed in the operation use, each of them is facing their own challenge. 4D-Var requires coding the adjoint model, which is difficult to perform for complex systems. The CTM and CCMM are complex systems with rapid updates, and the implementation of 4D-Var requires a large workload of adjoint models coding (Ha, 2022). EnKF obtains a flow-dependent BEC using ensemble forecast by integrating the model multiple times, and that makes it approximately 100 times more computationally expensive than the forward model when applied to nonlinear systems (Counillon and Bertino, 2009). Notably, the problem of BEC forecasting in OI and 3D-Var is solved by EnKF using a Monte Carlo approach. EnKF obtains the forecast ensemble by integrating the model multiple times and uses the empirical covariance of the forecast ensemble to update all ensemble members to obtain the analysis ensemble. When the number of ensemble members tends to infinity, the empirical covariance of the forecast ensemble approximates the true value of the forecast error covariance. Compared with variational assimilation, EnKF has a flow dependent BEC and does not require an adjoint model, which is an advantageous data assimilation method. Several studies applied EnKF to assimilate surface or satellite observations to improve the CTM model forecast accuracy. For example, Lopez Restrepo et al. (2020) calibrated the spatial length scale of the covariance localization and the temporal length scale of the stochastic model for the emission uncertainty of EnKF and assimilated ground level PM<sub>2.5</sub> and PM<sub>10</sub> data with an optimized assimilation system to improve the simulation and forecasting of PM<sub>2.5</sub> and PM<sub>10</sub> in a densely populated urban valley of the tropical Andes. Park et al. (2022) developed a DA system for the CTM using the EnKF technique, where PM<sub>2.5</sub> observations from ground stations are assimilated to ICs every 6 hours to improve PM<sub>2.5</sub> forecasting in the Korean region. Peng et al. (2017) used EnKF to optimize ICs and emission input, resulting in significant improvements in PM<sub>2.5</sub> forecast. However, EnKF also requires an appropriately sized ensemble. A small ensemble introduces significant sampling error, while an excessive ensemble consumes considerable computational resources.

For low dimensional linear dynamical systems, standard techniques are used to achieve DA, such as KF, or the adjoint methods. However, the CTMs are strongly nonlinear systems, and the assumptions of Gaussian variables and non-biased do not apply. Advanced DA techniques such as 4D-Var, EnKF are approximately 100 times more computationally expensive than the forward model when applied to nonlinear systems (Counillon and Bertino, 2009). Moreover, the Coupled chemistry meteorology models (CCMM) are CTMs that simulate meteorological processes and chemical transformations jointly, with model computations far exceeding those of equivalent weather models, and it will be a great challenge to establish a real time and operational DA system. Compared to EnKF, EnOI is a suboptimal method for ensemble-based assimilation (Evensen, 2003). EnOI uses a stationary ensemble to estimate the BEC and only one analysis field (AF) is updated at a time, which makes the computation time greatly reduced. EnOI is robust, flexible, portable, and inexpensive, and is not burdened with the technical difficulties that some other methods carry. EnOI can be used in conjunction with other DA methods and may be an appropriate choice for coupled forecast systems (Oke et al., 2010). EnOI has been widely used in ocean models with significant improvements to model forecast (Counillon and Bertino, 2016; Castruccio et al., 2020; Xie and Zhu, 2010; Belyaev et al., 2021), but not in the CTM or CCMM. actual operational use in CTMs is still relatively rare. To our knowledge, there are only several papers involved researches of EnOI in atmospheric chemistry models so far. Zhang et al. (2014) implement the EnOI

on an air quality numerical modelling MM5-STEM for the Pearl River Delta region in China. They found that EnOI produced the initial condition closer to the true situation, but they didn't investigate the effect of EnOI on forecast. Wang et al. (2016) used EnOI to investigate the possibility of optimally recovering the spatially resolved emissions bias of black carbon aerosol. Kong et al. (2021) applied EnOI to assimilate hourly surface observations of CO concentrations at 1107 sites over China in January 2015. They found that simulations with the updated emissions revealed a decrease bias of average CO concentrations at 349 independent validation sites from  $0.74 \text{ mg m}^{-3}$  to  $0.01 \text{ mg m}^{-3}$  and a reduction of the RMSE by 18%. Results from these papers showed that EnOI is a useful and computation-free method to reduce the errors of initial chemical condition or emissions. Since development of CCMM are fairly recent, EnOI have not applied for real-time CCMM yet. The GRAPES-CUACE is an online CCMM system developed by the China Meteorological Administration (Gong and Zhang, 2008; Zhou et al., 2008; Wang et al., 2010a). This model not only plays an important role in the scientific research on air pollution (Wang et al., 2015a; Wang et al., 2015b), aerosol-cloud interaction (Wang et al., 2018; Peng et al., 2022); and aerosols' weather feedback (Wang et al., 2010b; Zhang et al., 2022), but is also applied for the operational forecasting of air quality, Fog-Haze weather and dust storm in China (Wang and Niu, 2013; Liu et al., 2017). Very recently, this model system has been updated to a new version (GRAPES Meso5.1/CUACE) with many improvements (Wang et al., 2022). In this study, we established a real-time EnOI chemistry initial fields  $\text{PM}_{2.5}$  assimilation system for ~~this new version of model GRAPES Meso5.1/CUACE to~~ with assimilating  $\text{PM}_{2.5}$  data from nearly 1500 ground stations in China into the model chemical initial fields to improve the model forecasts of the concentrations of  $\text{PM}_{2.5}$  ~~PM<sub>2.5</sub> forecast accuracy~~ and discuss the impact of assimilating  $\text{PM}_{2.5}$  on visibility.

## 2 Methods and Data

### 2.1 ~~EnOI~~ The ensemble optimal interpolation algorithm

~~DA methods are algorithms for optimal estimation. They combine observations and model results and their respective statistical characteristics of errors to obtain a statistically optimal analysis value by minimizing the analysis variance. Based on Kalman filter theory, the sequential assimilation methods use Eq. (1) to update the state variables.~~

~~$$\mathbf{x}^a = \mathbf{x}^b + \mathbf{K}(\mathbf{y} - \mathbf{H}(\mathbf{x}^b)) \quad (1)$$~~

~~Where the model forecast and analysis are denoted as  $\mathbf{x}^a$  and  $\mathbf{x}^b$ , respectively, and the measurements are contained in  $\mathbf{y}$ . The observation operator  $\mathbf{H}$  is the spline or other interpolations from the initial fields  $\text{PM}_{2.5}$  to the observational space.  $\mathbf{K}$  is the Kalman gain matrix.  $\psi_i = (i = 1, \dots, N)$  is an n dimensional model state vector representing members of the ensemble. N ensemble samples are combined in an ensemble  $\mathbf{A}$ .~~

~~$$\mathbf{A} = (\psi_1, \psi_2, \dots, \psi_N) \in \mathbb{R}^{n \times N} \quad (2)$$~~

~~$$\bar{\mathbf{A}} = \mathbf{A} \mathbf{E}_N \in \mathbb{R}^{n \times N} \quad (3)$$~~

~~Where  $\bar{\mathbf{A}}$  is the ensemble mean, and the ensemble anomaly  $\mathbf{A}'$  is then defined as~~

$$A' = A - \bar{A} = A(I - E_N) \in \mathfrak{R}^{n \times N} \quad (4)$$

Where  $E_N$  is an  $N \times N$  matrix with each element being  $1/N$ .

EnOI is approximate to EnKF. This involves using a stationary historical ensemble to define BEC matrix  $B$ .

$$B = \frac{A' A'^T}{N-1} \in \mathfrak{R}^{n \times n} \quad (5)$$

165 As in Evensen (2003), the EnOI analysis is computed by solving an equation written as:

$$\psi^a = \psi^f + \alpha(A' A'^T) H^T [(\alpha H(A' A'^T) H^T + (N-1)R)]^{-1} (d - H\psi^f) \quad (6)$$

The analysis is now computed to update only one model state at a time. As in Eq. (1),  $\psi^a$  is the AF,  $\psi^f$  is background field (BF),  $d$  is the measurements,  $R$  is the measurement error covariance.  $(d - H\psi^f)$  is the forecast innovation. A scalar  $\alpha \in (0, 1]$  is used to adjust the weight between the measurement and the ensemble, and  $\alpha$  is taken as 0.9 in this study. EnOI

170 algorithm used in this study is based on the work of Evensen (2003). A brief recall of the EnKF and EnOI is given in this section. DA methods are algorithms that combine observations and model results and their respective statistical characteristics of errors to obtain a statistically optimal analysis value by minimizing the analysis variance. Based on Kalman filter theory, the analysis state  $\psi^a$  is determined by a linear combination of the vector of measurements  $y$  and the forecasted model state vector or background  $\psi^f$ , which is given by the equation (1) and (2),

$$175 \quad \psi^a = \psi^f + K(y - H\psi^f) \quad (1)$$

$$K = PH^T [HPH^T + R]^{-1} \quad (2)$$

where  $K$  is Kalman gain matrix,  $P$  is the background error covariance matrix,  $H$  is the observation operator that relates the model state to the observation, and  $R$  is the observation error covariance matrix.

Now we define  $A$  is the matrix holding the ensemble members  $\psi_i$

$$180 \quad A = (\psi_1, \psi_2, \dots, \psi_N) \in \mathfrak{R}^{ndim \times N} \quad (3)$$

where  $N$  is the number of ensemble members and  $ndim$  is the size of the model state vector

let  $\bar{A}$  be the ensemble mean of  $A$ , then the ensemble anomaly  $A'$  is defined as

$$A' = A - \bar{A} \quad (4)$$

The ensemble covariance matrix  $P$  can be defined as

$$185 \quad P = \frac{A' A'^T}{N-1} \in \mathfrak{R}^{ndim \times ndim} \quad (5)$$

the vector of measurements  $y$  need to be perturbed with its error as the following

$$d_j = y + \varepsilon_j, \quad j = 1, \dots, N \quad (6)$$

which can be stored in a matrix as

$$D = (d_1, d_2, \dots, d_n) \in \mathfrak{R}^{m \times N} \quad (7)$$

190 where  $m$  is the number of measurements.

The EnKF analysis equation will be expressed as the following

$$\mathbf{A}^a = \mathbf{A} + \mathbf{A}'\mathbf{A}'^T\mathbf{H}'^T[(\mathbf{H}\mathbf{A}'\mathbf{A}'^T\mathbf{H}'^T + (\mathbf{N} - 1)\mathbf{R})]^{-1}(\mathbf{D} - \mathbf{H}\mathbf{A}) \quad (8)$$

195 The analysis includes updating each ensemble and need to run the model  $N$  times in every forecast cycle to calculate  $\mathbf{P}$ , therefore tends to be computationally demanding and has limited use when the computer time is the main affecter to be considered, especially in real-time operational forecast.

The EnOI analysis is computed with the ensemble covariance matrix  $\mathbf{P}$  spanned by a stationary ensemble of model states sampled from a long-time integration. It is computed by solving an equation written as the following

$$\boldsymbol{\psi}^a = \boldsymbol{\psi}^f + \alpha\mathbf{A}'\mathbf{A}'^T\mathbf{H}'^T[(\alpha\mathbf{H}\mathbf{A}'\mathbf{A}'^T\mathbf{H}'^T + (\mathbf{N} - 1)\mathbf{R})]^{-1}(\mathbf{y} - \mathbf{H}\boldsymbol{\psi}^f) \quad (9)$$

200 where the scalar  $\alpha \in (0, 1]$  is introduced to allow for different weights on the ensemble versus measurements. As Evensen (2003) pointed out, an ensemble consisting of model states sampled over a long time period will have a climatological variance which is too large to represent the actual error in the model forecast, and  $\alpha$  which mainly depends on how the model forecast behaviours is used to reduce the variance to a realistic level and can be tuned for optimal performance. In this study, it is taken as 0.9 based on our experience.- Through Eq.(Eq. (9)) the EnOI analysis updates only one model state at a time, so the computer time can be reduced by one or two orders of magnitude.

## 205 **2.2 The EnOI data assimilation system design**

Using a set of ensemble forecasts with finite number to calculate the BEC will suffer from sample error and cause imperfect estimation or even filter divergence (Houtekamer and Mitchell, 1998). There are two sorts of techniques to possibly solve this problem. One is the distance-dependent covariance localization, which is done by updating the analysis at all grid points with the multiplication of the BEC by a correlation function (Hamill et al., 2001). The other is done by updating the analysis at each  
210 grid point simultaneously using the state variables and the observations in the local region centred at that point (Ott et al.2004). In our EnOI DA system, we use the second technique. First, we define the localization length-scale as  $L$ . For each model grid point, we find the observations within  $L$  which are called active observations, and then calculate the corresponding innovation. This localization effect on the analysis is illustrated in section 3.1 (Fig.3).

The observation error covariance matrix  $\mathbf{R}$  is assumed to be diagonal here, that is, the observation errors are not correlated.  
215 The diagonal elements of  $\mathbf{R}$  are thus given by the sum of the measurement error variance  $\varepsilon_o^2$  and representativeness error variance  $\varepsilon_r^2$ , following Elbern et al. (2007). The measurement error-  $\varepsilon_o$  is assigned as 7.5% of observed value, and representativeness errors  $\varepsilon_r$  is formulated as  $\varepsilon_r = \varepsilon_o \cdot \sqrt{\frac{\Delta x}{L_r}}$ , where  $\Delta x$  is model grid resolution (10km in this study) and  $L_r$  is the characteristic representativeness length of the observation, defined as 2 km for urban sites, 10km for rural sites and 20km for remote sites, respectively.

220 Based on the ~~EnOI~~Eq. (69), we built the EnOI initial field PM<sub>2.5</sub> assimilation system, as shown in Fig. 1. The main procedures can be divided into pre-processing, analysis, and post-processing. Pre-processing involves the acquisition of observed data and ensemble samples. Analysis is the revised main module of EnOI where the main computational processes are performed. Post-processing firstly verifies the assimilation results using the validation observations which are not used in EnOI and then processes the results obtained from assimilation into model-readable chemical ICs to preliminarily verify the assimilation  
225 results/initial conditions. Compared with the traditional EnOI, the time-continuous model historical forecasts ~~samples~~ before the assimilation moment are selected as the ensemble samples for this study. The ensemble design is set to be as following: suppose the assimilation will be done at time t, first we evolve the model from the spin-up run at t-NΔt and integrate the model to time t (in our operational set up, Δt is 1 hour), therefore we get a time series of N hourly model forecast outputs A<sub>t-N+1</sub>, A<sub>t-N+2</sub>, ..., A<sub>t-1</sub>, A<sub>t</sub>. These hourly outputs before the assimilation time t form the N-number ensemble A, which can be used to calculate the average  $\bar{A}$  and anomalies  $A'$  and then the background error covariance matrices  $P$  is calculated. The BEC is stationary for  
230 a particular analysis moment, but it changes with the assimilation moment during a long assimilation period. Because background error covariance statistics are derived directly from forecasts and the DA scheme does not need to modify the original CCMM, EnOI is very easy to apply and very cost-free in term of computation time.

## 235 **2.23 GRAPES\_Meso5.1/CUACE**

In this study, the DA method EnOI was established for the latest updated version of the regional atmospheric chemistry model GRAPES\_Meso5.1/CUACE developed by the China Meteorological Administration (Wang et al., 2022). The model has been widely used to study dust and haze prediction, aerosol radiation, and aerosol cloud interactions (Wang et al., 2008; Wang et al., 2010a; Wang et al., 2010b; Wang and Niu, 2013; Wang et al., 2015; Zhou et al., 2012; Wang et al., 2018; Peng et al., 2020; Peng et al., 2021a; Zhai et al., 2018; Zhang et al., 2022).  
240 The model system consists of two main components, which are called GRAPES\_Meso and CUACE, respectively. GRAPES\_Meso refers to a real-time operational weather forecasting model used by China Meteorological Administration (Chen et al., 2008; Zhang and Shen, 2008). Now, the new version of it has been established with the resolutions ranging from 3 to 10 km for regional forecast (Shen et al., 2020). It uses fully compressible non-hydrostatic equations as its model core. The vertical coordinates adopt the height-based, terrain-following coordinates, and the horizontal coordinates use the spherical coordinates of equal longitude-latitude grid points. The horizontal discretization adopts an Arakawa-C staggered grid arrangement and a central finite-difference scheme with second-order accuracy, while the vertical discretization adopts the vertically staggered variable arrangement. The time integration discretization uses a semi-implicit and semi-Lagrangian temporal advection scheme. The transport and advection processes for all gases and aerosols are calculated by the dynamic framework of it. The second component, CUACE, refers to the  
245 atmospheric chemistry model (the Chinese Unified Atmospheric Chemistry Environment model), which mainly includes three modules: the aerosol module (CAM), the gaseous chemistry module (RADM2) and the thermodynamic equilibrium module  
250



(ISOPIA). For the dynamic frame, the model uses a full compressible non-hydrostatic model core, an Arakawa C staggered grid, an improved material advection scheme of the Piecewise Rational function Method (Peng et al., 2005), and a height based terrain following coordinate. The chemical module uses the CUACE, which consists of an emission inventory system, CAM aerosols module, Regional Acid Deposition Model (RADM2) and gases particles transformation related processes. In the RADM2 module, 63 gas species through 21 photochemical reactions and 136 gas-phase reactions participate in the calculations. CAM module considers the dynamic, physical and chemical processes of aerosols including hygroscopic growth, dry and wet depositions, condensation, nucleation, [vertical mixing, cloud chemistry, and coagulation and activation of cloud condensation nodules from aerosols](#), etc (Gong and Zhang, 2008). Seven types of aerosols (sea salt, sand/dust, black carbon, organic carbon, sulfate, nitrate, and ammonium salt) are considered in the CAM. The aerosol size spectrum (except for ammonium salt) is divided into 12 bins with particles radius of 0.005–0.01, 0.01–0.02, 0.02–0.04, 0.04–0.08, 0.08–0.16, 0.16–0.32, 0.32–0.64, 0.64–1.28, 1.28–2.56, 2.56–5.12, 5.12–10.24, and 10.24–20.48  $\mu\text{m}$ . [The interface program that connects CUACE and GRAPES Meso transmits the meteorological fields calculated in GRAPES Meso and the emission data processed as needed to each module of CUACE. GRAPES Meso and CUACE are online fully-coupled \(Peng et al., 2021; Zhang et al., 2022\).](#)

## 2.3.4 Data used

[Based “Ambient air quality standards” \(GB 3095-2012\) of China, the mass concentration limit of  \$\text{PM}\_{2.5}\$  and its corresponding air quality level and air pollution index \(API\) are shown in Table 1. Haze is defined as a weather phenomenon caused by air pollution when visibility is less than 10km, according to “Observation and forecasting levels of haze” \(QX/T 113-2010\) of China. Three pollution episodes occurred in China in December 2016, with the most severe haze episode occurring in China](#) [A severe haze episode occurs in Northern China](#) from 16~~5~~<sup>3</sup> December 2016 (see more details in Wang et al. 2022, Table 3).- During this pollution episode, the highest daily  $\text{PM}_{2.5}$  concentration peaks 600  $\mu\text{g m}^{-3}$  in Shijiazhuang and some other cities, reaching the severely polluted level (250-500  $\mu\text{g m}^{-3}$ ).- In this study, [15-23 December this regional haze episode 2016](#) was selected as the [main](#) study period, and both model input data and observation data used in this study are within this [period month](#). Model input data include anthropogenic emission data, model meteorological initial and boundary data. The emission inventory used in this study is from the Multi-resolution Emissions Inventory for China (MEIC) in December 2016 (<http://www.meicmodel.org/>). The emission inventory covers power plants, industry (cement, Iron and steel, industrial boilers, petroleum industry), residential, transportation, solvent use and agriculture, in-field crop residue burning etc. National Centers for Environmental Prediction (NCEP) Final analysis (FNLs) data (<https://rda.ucar.edu/datasets/ds083.3/>) are used for the model’s initial and 6 h meteorological lateral boundary input fields. The observations include  $\text{PM}_{2.5}$  and visibility. Nearly 1500 ground-based hourly  $\text{PM}_{2.5}$  ( $\mu\text{g m}^{-3}$ ) observations from the Chinese Ministry of Environmental Protection, with the detailed location and spatial distribution of the stations shown in Fig. 4-2. The hourly meteorological automatic ground-based visibility data (km) were obtained from the China Meteorological Administration. The time format of these observations is processed to UTC and all the observational data are obtained after quality control and rechecked before use.

## 2.45 Experimental Setup

285 The horizontal resolution, time step, forecast length and model domain of the GRAPES\_Meso5.1/CUACE model are optional. In this study, the horizontal resolution of the model is  $0.1^{\circ} \times 0.1^{\circ}$ , the time step is 100 s considering model integration stability and accuracy, and the model domain is  $15-60^{\circ}$  E,  $70-145^{\circ}$  N and (grey dashed box in Figure 2). There are 49 model layers ascending vertically from the surface to 31km in height. The model warm restart time is 0000 UTC and 1200 UTC, and the forecast length is 24 hours. The ~~chemical initial field of the model warm restart uses the 24-hour forecast field of the day before the model, or the chemical initial field assimilated by EnOI, and the model~~ simulation results are output on an hourly basis.

290 Three groups of experiments were performed in this study: one set of control experiments (CR), one set of sensitivity experiments and one set of cyclic DA experiments, as shown in Table 1. CR00 is the control experiment representing model run without DA begin at 0000 UTC every day and forecast 24 hours~~the model with a daily warm restart at 0000 UTC and without DA~~ (the initial field is the previous day's 24-hour forecast field), simulated from ~~91 to 2331~~ December 2016. CR12 is also model run without DA but begins at 1200 UTC every day and forecast 24 hours.

295 The localisation length-scale L and the ensemble size N are the key parameters affecting EnOI. Based on CR00, two parallel sensitivity experiments were designed to study the impact of localisation length-scale and ensemble size on the assimilation effects. The chemical initial fields, ensemble samples for the sensitivity experiments were obtained from the CR00. The first group of sensitivity experiments is fixed with ensemble size N of 48, and length-scale is selected for 20, 40, 60, 80, and 100 km to investigate the impacts of

300 different localization length-scale choices on the optimized chemical initial field; the second group is fixed with length-scale L of 80 km, and the 24, 48, 72, 96, 120, and 144 simulations before the assimilation moment (0000 UTC) were selected as ensemble samples, respectively, and the effect of the number of ensemble samples on the assimilation effect was discussed. ~~Considering that the missing localization could break the model dynamical balance(Oke et al., 2007), localization was performed in selecting the optimal ensemble size.~~

305 To investigate the impact of the assimilation moment on the forecast fields, the optimal length-scale and ensemble size were selected based on the results of sensitivity experiments, and two sets of cyclic DA experiments, DA00 and DA12, were set up to represent the daily assimilation of the initial fields at 0000 UTC and 1200 UTC, respectively. The N hourly model forecasts before the assimilation moment were used as the ensemble samples to approximate the BEC, and the analysis increments are calculated by combining the model forecasts and PM<sub>2.5</sub> observations at 0000 UTC and 1200 UTC, and the revised AFs analysis

310 are used as the chemical initial fields for the next forecast to achieve cyclic DA. ~~To avoid errors caused by different warm restart times, the CR12 control experiment is set up to represent a daily warm restart at 1200 UTC but without assimilation to be used as a reference experiment for DA12.~~

### 3 Result and discussion

#### 3.1 Localization length-scale sensitivity experiments

315 ~~The aspect of localisation needs to be adapted for specific applications~~The localization effect on the analysis is illustrated  
~~firstly and,~~so two observation sites A (114.5° E, 38.0° N), and B (36.6° N, 116.9° E) were selected to perform a length-scale  
single-point experiment for the initial field at 0000 UTC on 15 December 2016, corresponding to the left and right columns of  
the analysis increments ( $\psi^a - \psi^f$ ) shown in Fig. 3. The analysis increments are determined by both the observation increments  
and the BEC based on Eq. (69). As shown in Fig. 3, the increments are positive in the left and negative in the right column,  
320 which represent the underestimation of PM<sub>2.5</sub> concentration at site A and overestimation at site B before being assimilated. As  
the length-scale increases, the range of analysis increment expands, and the number of model grids that can be affected  
increases gradually. Due to the sparse distribution of PM<sub>2.5</sub> sites, if the localization length-scale is too small, most of the model  
grids cannot be updated, which reduces the assimilation efficiency; whereas if the localisation length-scale is too large, the  
analysis increments between distant sites will offset and superimpose, creating fake increments. With the experiments using  
325 length-scale of L = 80 and 100 km, a small negative analysis increments are found at site A in the southeast direction. Compared  
to site A, a wide positive analysis increments that do not match the actual situation are found at site B in the west direction for  
experiments using L=60, 80, and 100km. ~~Clearly too large a localization radius can lead to error increments.~~It is worth noting  
that there are differences in the shape of the analysis increment fields at sites A and B, which is related to the EnOI having a  
flow-dependent BEC, the details of BEC will be discussed in 3.2.

330 Ground-based PM<sub>2.5</sub> sites are established according to the population and economic development level of the region, and are  
not evenly distributed, such as Beijing, Shanghai, Guangzhou, and other economically developed and populous megacities,  
which have a high density of PM<sub>2.5</sub> sites, while the western and central regions of China are sparsely populated, and the sites  
are partially sparse. So, in order to obtain the statistically optimal localization length-scale, we performed assimilation  
experiments on the initial fields at 0000 UTC each day from 1 to 31 December. 50% of PM<sub>2.5</sub> sites were randomly selected as  
335 DA sites, and the rest were used as verification sites (without DA), and the blue and brown sites shown in Fig. 2 represent the  
spatial distribution of verification and assimilation sites, respectively. ~~the initial fields from 15 to 23 December 2016 were  
performed for sensitivity experiments, respectively, and~~the statistics results of verification sites against the observation are  
shown in ~~Fig. 4~~Table 3. ~~The more the scatter points are clustered on the diagonal line means that more the simulation is closer  
to the observation.~~ Compared to the CR, ~~the scatter distribution of the DA experiments is closer to the diagonal, with~~  
340 Correlation Coefficient (CORR) of DA for verification sites increase from 0.65 to 0.77 at least, and the Root Mean Square  
Error (RMSE), Mean Bias (MB), and Mean Error (ME) of the DA experiment are smaller than those of the CR. The statistical  
data are different for different Localisation length-scale, indicating that localization can have an effectively on the assimilation.  
Compared with the CR, RMSE of DA decreased from 60.1 to 41.6  $\mu\text{g m}^{-3}$ , MB decreased from 8.5 to 3.2  $\mu\text{g m}^{-3}$  and ME  
decreased from 41.73 to 25.9  $\mu\text{g m}^{-3}$  for the localization length-scale selection of 40 km. ~~When localisation is used with a 40-~~  
345 ~~member ensemble and length scale of 40km, the RMSE is 18.472  $\mu\text{g m}^{-3}$ , ME is 10.481  $\mu\text{g m}^{-3}$ , and CORR is 0.977, which is~~

the best among all the experiments on different length-scale. ~~Localisation length-scale of 60km and 80km have similar statistics results, but the statistics of 20km and 100km are not very good. For experiments with length scale of 20, 40, 60, 80 and 100 km MB is 2.656, 1.973, and 1.928, 2.194, 1.985  $\mu\text{g m}^{-3}$ , respectively. Ground-based  $\text{PM}_{2.5}$  sites are established according to the population and economic development level of the region, and are not evenly distributed, such as Beijing, Shanghai, Guangzhou, and other economically developed and populous megacities, which have a high density of  $\text{PM}_{2.5}$  sites, while the western and central regions of China are sparsely populated, and the sites are partially sparse.~~ Using a localization length-scale of 20 km prevents most of the model data from being updated while using too large a length-scale allows remote sites to interact with each other and produce more spurious increments. In addition, from the meteorological conditions, heavy pollution weather is always characterized by small or static winds, pollutant transport over small distances, an observation site represents a limited spatial extent, so a larger localized length-scale setting may also not produce an very realistic unreasonable initial field. ~~In summary, we concluded that the best assimilation effect can be achieved.~~ From this sensitivity experiment, we find that when the localization length-scale is using from 40 km to 80km, the statistics are relatively good and the optimal assimilation effect can be achieved.

### 3.2 Ensemble size sensitivity experiments

We repeat the series of experiments presented in Fig. 3, but with a localising length-scale of 80 km and 24, 48, 72, 96 and 120 ensemble members. Figure 54 shows a map of BEC CORR correlation field between observation sites (A, B) ~~and BECs~~ for different ensemble size, overlaid with the 0000 UTC surface wind vector of 15 December 2016. Site A is controlled by strong north and northwest winds, which makes the ~~±CORR~~ field show a northeast-southwest trend; The wind speed at site B is less than  $5 \text{ m}\cdot\text{s}^{-1}$  in all directions with a steady state, so the CORR field is approximately distributed in concentric circles nearby the center of the site. ~~As the number of ensemble samples increases, the area of positive CORR greater than 0.7 gradually increases in A and B, the range of positive CORR at sites A and B gradually increases with the range of CORR greater than 0.7.~~ The ensembles of size  $N=24$  or  $N=48$  can be considered small compared to the selection of other ensemble sizes in sensitivity experiments. In this case, the CORRs between the observation sites and the surrounding large-scale areas are all greater than 0.7, and an extremely strong negative correlation is found in the southwest, ~~which exaggerates the correlation of each area.~~ The success of ensemble-based DA systems depends strongly on the number of samples. The smaller ensemble size fails to accurately estimate the BEC and is prone to sampling error, resulting in an overestimation or underestimation of the initial field unreasonable results, and Natvik and Evensen (2003) investigated the effect of the number of samples on assimilation and showed that an ensemble of fewer than 60 samples reduce the performance of assimilation. When the hourly model forecasts of over 5 days ( $N=120$ ) before assimilation are selected as the ensemble samples, the correlations of both sites A and B with the BECs in a wide area become positive.

~~Next, all  $\text{PM}_{2.5}$  sites were used to assimilate the initial field at 0000 UTC per day for this pollution episode, and six different ensemble sizes were used to improve the initial field as shown in Table 2. Compared with the unassimilated initial field, the RMSE, CORR, MB, and ME of the initial field after assimilation changed significantly. With only 24 ensemble samples~~

assimilated, the RMSE rapidly decreased from 71.776 to 20.675  $\mu\text{g m}^{-3}$ , and the CORR directly increased from 0.650 to 0.97, meanwhile the ME and MB were 1/4 and 1/9 of the original. When 120 samples were selected for assimilation, the analysis field  $\text{PM}_{2.5}$  statistics were worse than those of fewer samples (N=24, 48, 72, 96, 144). The RMSEs for 24, 120, and 144 samples were 20.675, 23.919, and 23.416  $\mu\text{g m}^{-3}$  respectively, and the CORRs were also less than 0.96, and the RMSE results for 48, 72, and 96 ensemble samples are 19.170, 18.908, and 18.849  $\mu\text{g m}^{-3}$  respectively. The DA sites were used to assimilate the initial field at 0000 UTC per day for December 2016, and six different ensemble sizes were used to improve the initial field as shown in table 4. Compared with the initial field without data assimilation, the RMSE, CORR, MB, and ME of the initial field after assimilation had all been improved and the improvement were different depending on the ensemble size. The priori initial field is shown in table 4 "CR". With only 24 ensemble samples assimilated, the RMSE of verification sites decreased from 60.1 to 48.6  $\mu\text{g m}^{-3}$ , the CORR increased from 0.56 to 0.76, and the MB and ME are decreased from 8.5 to 4.2  $\mu\text{g m}^{-3}$  and 41.7 to 30.8  $\mu\text{g m}^{-3}$ , respectively. As seen in table 3 the statistics of verification sites become progressively better as the ensemble members increases from 24 to 48, 72, and 96. The verification sites RMSEs for 48, 72, and 96 samples are 44.9, 42.4 and 40.70  $\mu\text{g m}^{-3}$  respectively, the CORRs are 0.80, 0.81, 0.82, and the MEs are 27.0, 25.9, and 25.7. When 120 samples or 144 samples were selected for assimilation, the analysis field  $\text{PM}_{2.5}$  DA and verification statistics were not better than those of 96 samples. The verification sites RMSEs for 120, and 144 samples were 44.1, and 45.8  $\mu\text{g m}^{-3}$  respectively, and the CORRs also became smaller. The differences between the statistics also indicate there is an optimal ensemble size, the RMSE of the experiment using 96 samples is smaller than the RMSE when using the other ensemble sizes, and the remaining statistics are better than the results when other samples are selected, so we consider that in this sensitivity experiments the best assimilation is achieved when the number of ensemble size is 96. It is noted from the experimental results that not the larger the ensemble, the better the results in this study. It could be influenced by the following reasons that the atmospheric chemistry model used in the study is coupled online with the mesoscale regional weather model GRAPES\_Mese5.1. The mesoscale regional weather model differs from the climate model and the global model in that the mesoscale model represents weather systems on time scales of one day to several days(Emanuel, 1986). In addition, atmospheric chemical processes are fast-varying processes with small time scales compared to climatic and oceanic processes, so using model results from long-time integrations as ensemble may average out the "error of the day" and will not be a very good assessment of model background errors.

### 3.3 Impact on initial fields

The optimal localization length-scale, ensemble size of 40 km and 96 were obtained by sensitivity experiments, respectively. In order to verify the assimilation effect and evaluate quantitatively the impact of the EnOI system on the initial fields, DA experiments with length-scale of L=40 and ensemble size of N= 96 was performed on the initial field at each 0000 UTC from 15 to 23 December 2016. The assimilated observations were obtained from the DA sites in Fig. 2, and the effect on both DA sites and verification sites are evaluated. Figure 5 shows the statistics for the two regions of the initial field, the China mainland, and North China. In China mainland, the CORRs of the verification sites and DA sites before assimilation were 0.60 and 0.58,

respectively, and the RMSEs were 73.9 and 73.4  $\mu\text{g m}^{-3}$ , respectively. After the DA sites were assimilated, the CORR of assimilated sites increased to 0.99 and the RMSE decreased to 14.5  $\mu\text{g m}^{-3}$ , and the CORR of verification sites increased to 0.84 and the RMSE decreased to 46.4  $\mu\text{g m}^{-3}$ , meanwhile the ME changes from 49.7 to 27.3  $\mu\text{g m}^{-3}$ . In North China, after the DA sites were assimilated, each statistic of the validation site also changed, with the CORR increasing from 0.53 to 0.87, RMSE decreasing from 105.5 to 65.7  $\mu\text{g m}^{-3}$ . Only 50% of the ground-based observation are assimilated and the statistics of the validation sites also have been improved. This experimental results prove that the DA system can indeed yield more accurate initial field with over 40% increase of CORR and 37% reduction of RMSE, firstly, an independence test with length-scale of  $L=40$  and ensemble size of  $N=96$  was performed on the initial field of 0000 UTC on 15 December 2016. The 50% of  $\text{PM}_{2.5}$ -sites were randomly selected as DA sites, and the rest were used as verification sites (without DA), and the blue and red sites shown in Figure 2 represent the spatial distribution of verification and assimilation sites, respectively. As shown in Figure 6, the CORRs of the verification sites and DA sites before assimilation were 0.441 and 0.470, respectively, and the RMSEs were 59.914  $\mu\text{g m}^{-3}$  and 62.783  $\mu\text{g m}^{-3}$ , respectively. After the DA sites were assimilated, the CORR of assimilated sites increased to 0.977 and the RMSE decreased to 14.140  $\mu\text{g m}^{-3}$ , also the CORR of verification sites increased to 0.734 and the RMSE decreased to 46.041  $\mu\text{g m}^{-3}$ . It is obvious that the assimilation corrected the initial  $\text{PM}_{2.5}$  concentration significantly, especially in the region underestimate, and assimilating not only produces mainly localized increment structures concentrated around the measurement sites, but also affects other areas.

As in sensitivity experiments, all  $\text{PM}_{2.5}$ -sites were used as DA sites to assimilate the initial fields in the CR00 experiment separately, but with a localization length scale of 40 km and an ensemble size of 96. To understand/illustrate the assimilation effect of different pollution levels, we consider this episode from 15 to 23 December 2016, in which the first two days as the pollution start period, days 3 to 7 as the pollution period, and the last two days as the pollution dissipation period. We compared the  $\text{PM}_{2.5}$  observations and initial conditions before and after DA within all the observations sites assimilated during this episode. This was done to understand the impact of DA for initial conditions in the system's actual operating situation. In this section, we show in Fig. 7-6 shows the spatial distribution of  $\text{PM}_{2.5}$  in the observation field (OB), background field (BF), analysis field (AF), and analysis field increments (AFI) for two days of light pollution (16 and 23 Dec.) and two days of heavy pollution (19 and 20 Dec.). The black boxed area in Fig. 7-6 is the same as North China (NC) in Fig. 2, including Beijing, Tianjin, eastern Shanxi, southern Hebei, western Shandong, and northern Henan, which has the highest simulated  $\text{PM}_{2.5}$  concentration. Table 5 summarizes the corresponding statistics of initial  $\text{PM}_{2.5}$  concentrations for assimilation sites and verifications sites before and after EnOI. Fig. 6 shows that, compared with OBs, the model background  $\text{PM}_{2.5}$  without DA can capture the spatial pattern of distribution over China in generally which shows that the model performance is moderate good. However, there are still errors between the background and observations.  $\text{PM}_{2.5}$  concentrations are overestimated in NC and eastern China during the pollution start and dissipation periods. During the heavy pollution period, the BFs-background  $\text{PM}_{2.5}$  concentrations are overestimated in northeast China and underestimated in NC. After assimilating the BFs ground-based  $\text{PM}_{2.5}$ , the  $\text{PM}_{2.5}$  concentration increments were distributed around the observation sites as expected and distribution changes from sheet like to discrete, were more closer to the observations distributions, which is due to the update of the model data in

a length-scale of 40 km range with the distribution of observation sites, resulting in the adjustment of the  $PM_{2.5}$  in the BFs. Negative values of the AFI demonstrate that assimilation reduces  $PM_{2.5}$  concentrations, while positive values demonstrate that assimilation increases  $PM_{2.5}$  concentrations. During the period before and after pollution,  $PM_{2.5}$  concentrations decrease in eastern China and increase in western China and NC, indicating a reduction in over- or under-prediction of model  $PM_{2.5}$  concentrations after assimilation, indicating that the reduction of the overestimation or underestimation of the model simulation over these regions with data assimilation. Table 5 shows that assimilating 50% of the ground-based observations improved the initial condition for other areas where have no assimilated sites. Take 19 Dec. 2016 as an example, the CORR for verification sites increased from 0.66 to 0.85, RMSE decreased from 79.2 to 56.1  $\mu\text{g m}^{-3}$ , and MB and ME also became smaller after EnOI. These results indicate that the initial  $PM_{25}$  fields can be adjusted efficiently by EnOI. What is the impact of this innovation through the EnOI system for  $PM_{2.5}$  forecast is discussion in the next section.

To evaluate quantitatively the impact of the ensemble assimilation system on the initial fields, the RMSEs, MEs, MBs and CORRs of the assimilated initial fields and the BFs were first analysed. Table 3 shows the statistics for the two regions of the initial field, the China mainland (Total) and NC (Contains observation sites in NC). In China mainland, ME, and RMSE decreased by 75.53%, 72.33%, respectively, and CORR increased to 0.967. The MB changes from negative to positive, meanwhile the MB in mainland China becomes larger. In NC, MB decreased by 109.63%, ME decreased by 79.59%, RMSE decreased to about 20  $\mu\text{g m}^{-3}$ , and CORR increased by 148.59%. The results show that the correction effect of DA on the initial fields is evident.

### 3.4 Impact on forecast fields

#### 3.4.1 Impact on $PM_{2.5}$ forecast fields

In this section, we will investigate the performance of assimilating the initial field at 0000 UTC per day (DA00) or 1200 UTC per day (DA12) on improving the  $PM_{2.5}$  forecasts, with an example in North China (Figure 8), and the same study period as in section 3.3 was selected, DA00 (Figure 8 First and second rows) and DA12 (Figure 8 third and fourth rows) were performed in parallel. In NC, compared with the observations (brown line with circles), the forecast  $PM_{2.5}$  concentrations (black line, grey line) are 20 to 100  $\mu\text{g m}^{-3}$  higher in the pollution start period (16 December) and the pollution fading period (23 December), lower in the pollution period (19 December), and relatively consistent in (20). The daily trend of  $PM_{2.5}$  changes immediately one hour after 0000UTC in DA00 (blue line) or 1200UTC in DA12 (pink line), and the assimilation forecast value rapidly approaches the observations, after that the DA experiment gradually overlaps with the CR experiments in the context of daily changes of emission. It can be seen from Fig. 8 that the RMSEs of the DA experiments (blue and pink lines marked with squares) are always lower than that of the CR experiments (black and grey lines marked with squares), which proves that assimilating the initial field improves the  $PM_{2.5}$  forecast field throughout the assimilation time window, yet the assimilation impact is strongest in the first 12 hours. The comparison reveals that the assimilation effect is related to the choice of the assimilation moment, and the blank area between the RMSE line of the DA experiment and the RMSE line of the CR

experiment represents the improvement of the DA on the forecast, and the larger the blank area is, the greater the improvement of the DA on the forecast. For example, the model forecast at 0000UTC on 19 December is closer to the observation, and assimilating the initial field at 0000UTC does not improve the model forecast significantly; instead, the model is about  $100 \mu\text{g m}^{-3}$  lower than the observation at 1200UTC, and the model's forecast improves more after assimilating the initial field at 1200UTC.

The daily average of the 24-hour RMSE was obtained for the DA and CR experiments, the relative RMSE was calculated and plotted in a daily time series histogram as shown in Fig. 9. The red and blue bars represent the percentage improvement of the original forecasts after assimilation, and the white diagonal bars represent the difference between the improvements of DA00 and DA12. In this episode, the improvement of China mainland  $\text{PM}_{2.5}$  forecasts by DA00 and DA12 are minimum at 9% and 10% respectively on December 15 and maximum at 15% and 21% respectively on December 19. The minimum and maximum improvement of assimilation on  $\text{PM}_{2.5}$  forecasts in NC both appear in DA12, which are 3% and 25%, respectively. The difference between DA12 and DA00 relative RMSEs is mostly positive, within 6% in China mainland, but in NC this difference can be up to 15%. The study shows that assimilating the initial field at 1200 UTC improves the  $\text{PM}_{2.5}$  forecast more than 0000 UTC, mainly because the model forecasts are not close to the observations at 1200 UTC in most cases (Figure 8), thus choosing this time for assimilation will have a significant impact. The selection of the assimilation moment can be disregarded in the case of abundant computing resources because, with the increase of assimilation frequency, it can also achieve good results, but in the case of limited computing resources, choosing the suitable assimilation moment can save computing resources as well as improve the forecast accuracy.

In this section, we will discuss the impact of assimilation observations on  $\text{PM}_{2.5}$  forecasts. As in Section 3.3, we assimilate the DA sites at 0000 UTC from 15 to 23 December 2016, and then analyse the following forecast of DA and the verification sites separately. The RMSE of the DA and verification sites in China mainland and North China for a complete pollution process obtained average over 15 to 23 December 2016 is shown in Fig. 7. For the DA sites in China mainland (Fig.7a), the model forecast RMSE without DA is about  $75 \mu\text{g m}^{-3}$ , after the assimilation, the model forecasts RMSE is decreased rapidly from 75.4 to  $40.1 \mu\text{g m}^{-3}$ , which is an over 40% reduction. This implies that assimilation with EnOI can considerably improve the forecast accuracy. Meanwhile, it is notable that assimilation of DA sites also has an impact on the forecast at the verification sites. The trend of the RMSE series at the verification site is consistent with the DA site, but smaller in values. The RMSE of verification sites at 1h forecast hour dropped from 75.5 to  $51.0 \mu\text{g m}^{-3}$ , about 32% reduction. For North China, which was shown in Figure7c and d, the model forecast RMSE without DA is about  $115 \mu\text{g m}^{-3}$ . After the assimilation of  $\text{PM}_{2.5}$  observation, the model forecasts RMSE of DA sites at 1h forecast time is decreased rapidly from 122 to  $56.1 \mu\text{g m}^{-3}$ , which is an over 54% reduction. For verification sites, the reduction amplitude is 33%, smaller than that of DA sites, but still a moderate improvement considering only 50% ground-based observations were used to be assimilated at 0000UTC. The results show that assimilation with EnOI not only improve the forecast for the DA sites but also the verification sites. The improvements are mainly within



515 the first 1224h forecasts with an RMSE greater than  $10 \mu\text{g m}^{-3}$ . The improvement receded with forecast time, changing from 46% at 1h forecast hour to 7% at 24h forecast hour. These results are consistent with previous study, which either used 4DVAR or EnKF (Wu et al. 2008; Bocquet et al, 2015, Park et al.,2022). As Bocquet et al. (2015) pointed out, even with the improved analysis, the impact of initial state adjustment is generally limited to the first day of the forecast, for pollutant transport and transformation are strongly driven by uncertain external parameters, such as emissions, deposition, boundary conditions, and meteorological fields.

520 Now we use all ground-based observation sites as DA sites to investigate the performance of assimilating the initial field at 0000 UTC per day (DA00) or 1200 UTC per day (DA12) on improving the  $\text{PM}_{2.5}$  forecasts. DA00 and DA12 were performed in parallel. The daily average of the 24-hour RMSE was obtained for the DA and CR experiments. Rate of improvement (ROI) by data assimilation in 1d (24h) predictions for 15 to 23 December 2016 for Mainland China and NC were calculated using the ratio of the reduced RMSE statistical metrics to those for the CR simulation and plotted in a daily time series histogram as shown in Fig. 8. In this episode, the improvement of China mainland  $\text{PM}_{2.5}$  forecasts by DA00 and DA12 are minimum at 9% and 10% respectively on December 15 and maximum at 15% and 21% respectively on December 19. The minimum and maximum improvement of assimilation on  $\text{PM}_{2.5}$  forecasts in NC both appear in DA12, which are 4% and 25%, respectively.

525 The difference between DA12 and DA00 relative RMSEs is mostly positive, within 6% in China mainland, but in NC this difference can be up to 15%. The average RMSE improvement of 24h forecast for China mainland and the North China assimilation at 0000 UTC is 12.3% and 9.8%, respectively, while that at 1200 UTC is 14.4% and 14.0%, respectively. In terms of the average relative RMSE for this episode, assimilating the initial field at 1200 UTC improves the  $\text{PM}_{2.5}$  forecast more than 0000 UTC, mainly because the model forecasts are not close to the observations at 1200 UTC in most cases, thus choosing this time for assimilation will have a significant impact. In addition, the DA effect varies for each day and the larger the error, the greater the improvement in RMSE from DA, which means that the larger the a priori error, the greater the improvement from DA. These results show that using EnOI to assimilate ground-based  $\text{PM}_{2.5}$  observations for the model chemical initial field can reduce over 9.8% of RMSE for 24h forecast in average. Park et al. (2022) implemented an ensemble Kalman filter in the Community Multiscale Air Quality model (CMAQ model v5.1) for data assimilation of ground-level  $\text{PM}_{2.5}$ . They found using EnKF with 40 ensemble number can reduce 9.6% of RMSE for 24h forecast. Comparing their results with ours, we can find that, while EnOI is sub-optimal, it can give improvement of forecast that are comparable to those of the EnKF. Moreover, the computational cost of EnOI is typically about N times less than that of EnKF. Therefore, we suggest that EnOI may provide a practical and cost-effective alternative to the EnKF for the applications where computational cost is a main limiting factor, especially for real-time operational forecast.

540 To achieve better performance of assimilation, we update the initial field every 12h. Figure 9 gives time series of forecasts and observations in term of  $\text{PM}_{2.5}$ , together with RMSE of CR and DA for North China. Compared with the observations, the forecast  $\text{PM}_{2.5}$  concentrations are 20 to  $100 \mu\text{g m}^{-3}$  higher in the pollution start period (15-17 December) and the pollution fading period (21, 23 December), about  $100 \mu\text{g m}^{-3}$  lower on December 19. The  $\text{PM}_{2.5}$  concentrations changes immediately one hour after 0000 UTC or 1200 UTC. It can be seen from Fig. 9b, the RMSEs of the DA experiments are always lower than

545 ~~that of the CR experiments, and the difference in RMSE between the CR and DA experiments receded with forecast time. This~~  
~~proves that assimilating the initial field can improve the PM<sub>2.5</sub> forecast. Note that the DA algorithm used here cannot produce~~  
~~an optimal solution when there are larger errors in the model. On 19 December 2016, even with DA the model still cannot~~  
~~retrieve the true variation very well for the first 12 hour forecast. -This suggest that using DA on initial field can only partially~~  
550 ~~remedy inherent model error. To improve the analysis capabilities and prolong the impact of DA on PM<sub>2.5</sub>AQ forecasts, we~~  
~~should extend the assimilation for adjusting emissions, meteorological field and other model uncertainty sources.~~

### 3.4.2 Impact on Visibility forecast fields

The occurrence of low visibility episodes is usually associated with aerosol pollution. The horizontal spatial distribution of the  
OBs, forecast fields without assimilation (CR), forecast fields with assimilation (DA), and incremental fields (DA-CR) for  
555 visibility and PM<sub>2.5</sub> at 0100 UTC on 16 and 20 December are shown in Fig.10. During the pollution start period (16 December  
0100 UTC) visibility is above 10km in most of China, and during the pollution period (20 December 0100 UTC) visibility is  
mostly below 7km in eastern China. After assimilating the ground-based PM<sub>2.5</sub>, the visibility distribution of DAs ~~becomes~~  
~~discrete~~ more consistent with the observation compared to the CRs. A positive PM<sub>2.5</sub> concentration increment corresponds to  
a negative visibility increment, that means that when the PM<sub>2.5</sub> concentration increases, the visibility decreases at the same  
560 moment. At 0100UTC On 16 December, the CR PM<sub>2.5</sub> concentration is underestimated in NC and overestimated in Southeast  
China, and after assimilating PM<sub>2.5</sub>, the visibility is reduced in NC with increased PM<sub>2.5</sub> and increased in Southeast with  
reduced PM<sub>2.5</sub>. In the period of light pollution, the absolute value of visibility increment is mostly in the range of 5-7 km when  
the PM<sub>2.5</sub> increment is from 30 to 110  $\mu\text{g m}^{-3}$  or from -30 to -110  $\mu\text{g m}^{-3}$  in NC, while in the pollution period (20 December  
0100 UTC for example), under the same PM<sub>2.5</sub> analysis increment, the visibility increment in NC is between -3 and 3 km. ~~It~~  
565 ~~proves that visibility is more correlated with PM<sub>2.5</sub> concentration when the pollution is lighter, while they are less correlated~~  
~~when the pollution is heavier, which is consistent with the findings of Yu et al. (2016) and Yadav et al. (2022).~~

Four stations, Beijing (BJ), Shijiazhuang (SJZ), Xingtai (XT), and Jinan (JN), were selected from the heavily polluted NC to  
study the effect of assimilating the initial field PM<sub>2.5</sub> on the visibility forecasts. Since the assimilation effect is most obvious  
in the first 12 hours, we focus on the improvement of visibility forecasts within 12 hours. Figure 11 shows the observation  
570 ~~(orange line)~~, simulation ~~(black dashed line)~~ and assimilation ~~(green line)~~ of visibility and observation ~~(grey line)~~, simulation  
~~(black line)~~ and assimilation ~~(blue line)~~ of PM<sub>2.5</sub> concentration for the above cities from 0100 to 1200 on 16 and 20 December  
2016. On 16 December, when PM<sub>2.5</sub> concentration is less than 300  $\mu\text{g m}^{-3}$  (December 16), visibility at all four stations is closer  
to the observed value by assimilating PM<sub>2.5</sub>, among which BJ and JN have decreased PM<sub>2.5</sub> concentration after assimilation,  
and visibility has increased at the same time. SJZ and XT have increased PM<sub>2.5</sub> concentration and decreased visibility after  
575 assimilation. In the period of low PM<sub>2.5</sub> concentration, about 100  $\mu\text{g m}^{-3}$  PM<sub>2.5</sub> change makes visibility change 11km, 4km,  
5km and 7km in BJ, SJZ, XT and JN respectively. In the period of heavy pollution, PM<sub>2.5</sub> concentration change 150  $\mu\text{g m}^{-3}$  in  
Beijing and Shijiazhuang at 0100UTC, while visibility change 3.5km and 0.5km respectively. ~~It is obvious~~ These result show

that the improvement of visibility by assimilating  $PM_{2.5}$  is limited during the heavy pollution period. It is worth noting that when the  $PM_{2.5}$  concentration is greater than  $350 \mu g m^{-3}$  at the JN site, although the decrease of  $PM_{2.5}$  concentration corresponds to the increase in visibility, the gap between the assimilated visibility and observation becomes larger at this time, which may be related to the inaccuracy of the humidity simulation here and inaccurate visibility parameterization scheme for the model. Visibility is not linearly related to  $PM_{2.5}$ , and visibility is also affected by humidity and other factors. Assimilation of the initial field  $PM_{2.5}$  can improve the visibility forecast, but if we want to improve the visibility forecast significantly, ~~other objects of assimilation, such as  $PM_{10}$ , humidity, etc., need to be considered.~~ we need to improve not only the visibility parameterization scheme, but also the humidity accuracy.

#### 4 Conclusions

To improve the accuracy of  $PM_{2.5}$  and visibility forecasting in China, a real-time and efficient EnOI assimilation system is established for the latest online operational chemistry weather model GRAPES\_Meso5.1/CUACE of China Meteorological Administration. The ground-based  $PM_{2.5}$  observation data nearly 1500 surface stations covering the whole country are used for assimilation.  $PM_{2.5}$  and visibility simulation-assimilation experiments were performed for a haze pollution episode from 15 to 23 December 2016. Parallel sensitivity experiments of localization length-scale and ensemble size were set up to determine two key parameters that influence the effectiveness of EnOI assimilation. Based on the results of sensitivity experiments, the initial fields were assimilated at 0000 UTC each day from 15 to 23 December 2016 to study the improvement of EnOI on the initial field  $PM_{2.5}$ . In addition to the analysis of the China mainland assimilation effect, the heavily polluted North China was additionally divided to discuss the different impacts of assimilation on the overall and regional chemical initial fields. Cyclic assimilation experiments were performed at 0000 UTC (DA00) and 1200UTC(DA12) to investigate the impacts of assimilation on the forecast fields, taking NC as an example, to discuss the impacts of assimilation on  $PM_{2.5}$  and visibility forecast fields.

The optimal localization length-scale and the number of ensemble samples are 40 km and 96, respectively, derived from sensitivity experiments. ~~The DA can significantly improve the model initial field, the AFs  $PM_{2.5}$  is more consistent with the observed results in both distribution and values. The AFs relative to the background fields (BFs) in China mainland, NC the ME decreased by almost 80%, the RMSE decreased by 72.33%, 75.53%, the CORR increased from 0.584 to 0.967, and 0.319 increased to 0.972.~~ Assimilating 50% of the ground-based observations improved the initial condition for other areas where have no assimilated sites. The DA can considerably improve the model  $PM_{2.5}$  initial field, the CORR of verification sites in mainland China improved from 0.58 to 0.84 and the RMSE decreased from 73.7 to 46.4  $\mu g m^{-3}$ , respectively. The results of the DA00, DA12 assimilation experiments showed that the improved impacts of the DA worked throughout the forecast time window, but the assimilation impact was most pronounced in the first 12 hours and gradually decreased in the subsequent time. Within the 24-hour forecast time window, the average RMSE improvement for the China mainland  $PM_{2.5}$  forecast field ranges from 9% to 21%, and between 4% and 25% in NC, and the comprehensive comparison shows that the initial field of 1200

610 UTC assimilation is superior to 0000 UTC. Therefore, in this study, it is considered that with limited computational resources, the EN<sub>1</sub>OI assimilation efficiency is highest with the largest distance between the model simulation and observation to assimilate according to the model characteristics. When it comes to operational use, the assimilation efficiency can be improved by shortening the assimilation time interval due to the small demand of EnOI computational resources.

615 The assimilation of PM<sub>2.5</sub> also has a ~~positive impacts~~~~significant improvement~~ on visibility forecasts, ~~with different degrees of visibility improvement in different cities~~. When the PM<sub>2.5</sub> increment by assimilation is negative, it corresponds to an increase in visibility, and when the PM<sub>2.5</sub> analysis increment is positive, visibility decreases correspondingly. The greater the change in PM<sub>2.5</sub> concentration during periods of light pollution, the more pronounced the improvement in visibility, ~~but this positive correlation is not particularly obvious during periods of heavy pollution. However,~~ ~~it~~ is worth noting that visibility is also related to a variety of factors ~~and~~. ~~A~~ assimilating only ground-based PM<sub>2.5</sub> sites has a limited effect on visibility, and we will  
620 further consider assimilating PM<sub>10</sub>, humidity and other meteorology factors to improve visibility forecasts in subsequent studies. ~~In addition, the number of ground based PM<sub>2.5</sub> sites is not large enough in most region of China, and we will consider assimilating PM<sub>2.5</sub> and satellite AOD data simultaneously at a later stage to achieve more accurate PM<sub>2.5</sub> and visibility forecasts.~~

*Code and data availability.* The EnOI method and related processes written in Fortran language and observation data used in  
625 this research are available at <https://doi.org/10.5281/zenodo.7002847>. The National Centers for Environmental Prediction Global Final Analysis (NCEP-FNL) data are available online (<https://rda.ucar.edu/datasets/ds083.2/> and <https://rda.ucar.edu/datasets/ds083.3/>). The emission inventories are available online (<http://www.meicmodel.org/>).

*Author contributions.* LST: Validation, Formal analysis, Writing - Original Draft, Visualization, Investigation, Software. WP:  
630 Conceptualization, Methodology, Software, Writing - Original Draft. WH: Conceptualization, Methodology, Supervision, Writing- Reviewing and Editing. PY: Validation, Software. LZD and ZWJ: Validation. LHL: Data Curation. WYQ and CHZ: Resources. ZXY: Supervision

*Competing interests.* The contact author has declared that neither they nor their co-authors have any competing interests.  
635

*Acknowledgements.* This study is supported by the National Key Research and Development Program (2019YFC0214603, 2019YFC0214601) and the NSFC for distinguished young scholars (41825011). We also appreciate the comments of the reviewers that helped us to improve this article.

## References

640 Belyaev, K., Kuleshov, A., Smirnov, I., and Tanajura, C. A. S.: Generalized Kalman Filter and Ensemble Optimal Interpolation, Their Comparison and Application to the Hybrid Coordinate Ocean Model, *Mathematics*, 9, 2371, 2021.

- Bergthórsson, P. and Döös, B. R.: Numerical Weather Map Analysis1, *Tellus*, 7, 329-340, <https://doi.org/10.1111/j.2153-3490.1955.tb01170.x>, 1955.
- 645 Cao, H., Henze, D. K., Zhu, L., Shephard, M. W., Cady-Pereira, K., Dammers, E., Sitwell, M., Heath, N., Lonsdale, C., Bash, J. O., Miyazaki, K., Flechard, C., Fauvel, Y., Kruit, R. W., Feigenspan, S., Brümmner, C., Schrader, F., Twigg, M. M., Leeson, S., Tang, Y. S., Stephens, A. C. M., Braban, C., Vincent, K., Meier, M., Seidler, E., Geels, C., Ellermann, T., Sanocka, A., and Capps, S. L.: 4D-Var Inversion of European NH3 Emissions Using CrIS NH3 Measurements and GEOS-Chem Adjoint With Bi-Directional and Uni-Directional Flux Schemes, *Journal of Geophysical Research: Atmospheres*, 127, e2021JD035687, <https://doi.org/10.1029/2021JD035687>, 2022.
- 650 Carnevale, C., De Angelis, E., Finzi, G., Turrini, E., and Volta, M.: Optimal Interpolation Based Data Fusion Techniques to Improve Deterministic Air Quality Forecast, *Air Pollution Modeling and its Application XXVII*, Berlin, Heidelberg, 2021//, 145-150.
- Castruccio, F. S., Karspeck, A. R., Danabasoglu, G., Hendricks, J., Hoar, T., Collins, N., and Anderson, J. L.: An EnOI-Based Data Assimilation System With DART for a High-Resolution Version of the CESM2 Ocean Component, *J. Adv. Model. Earth. Sy.*, 12, 10.1029/2020ms002176, 2020.
- 655 Cheng, Y., Dai, T., Goto, D., Schutgens, N. A. J., Shi, G., and Nakajima, T.: Investigating the assimilation of CALIPSO global aerosol vertical observations using a four-dimensional ensemble Kalman filter, *Atmos. Chem. Phys.*, 19, 13445-13467, 10.5194/acp-19-13445-2019, 2019.
- Counillon, F. and Bertino, L.: Ensemble Optimal Interpolation: multivariate properties in the Gulf of Mexico, *Tellus A*, 61, 296-308, 10.1111/j.1600-0870.2008.00383.x, 2009.
- 660 Counillon, F. and Bertino, L.: Ensemble Optimal Interpolation: multivariate properties in the Gulf of Mexico, *Tellus A*, 61, 296-308, 10.1111/j.1600-0870.2008.00383.x, 2016.
- Dai, T., Cheng, Y., Suzuki, K., Goto, D., Kikuchi, M., Schutgens, N. A. J., Yoshida, M., Zhang, P., Husi, L., Shi, G., and Nakajima, T.: Hourly Aerosol Assimilation of Himawari-8 AOT Using the Four-Dimensional Local Ensemble Transform Kalman Filter, *J. Adv. Model. Earth. Sy.*, 11, 680-711, 10.1029/2018ms001475, 2019.
- 665 Derber, J. C.: A Variational Continuous Assimilation Technique, *Mon. Weather Rev.*, 117, 2437-2446, 10.1175/1520-0493(1989)117<2437:Avcat>2.0.Co;2, 1989.
- Emanuel, K. A.: Overview and Definition of Mesoscale Meteorology, in: *Mesoscale Meteorology and Forecasting*, edited by: Ray, P. S., American Meteorological Society, Boston, MA, 1-17, 10.1007/978-1-935704-20-1\_1, 1986.
- Evensen, G.: Sequential data assimilation with a nonlinear quasi-geostrophic model using Monte Carlo methods to forecast error statistics, *Journal of Geophysical Research: Oceans*, 99, 10143-10162, <https://doi.org/10.1029/94JC00572>, 1994.
- 670 Evensen, G.: The Ensemble Kalman Filter: theoretical formulation and practical implementation, *Ocean Dynam.*, 53, 343-367, 10.1007/s10236-003-0036-9, 2003.
- Feng, S., Jiang, F., Jiang, Z., Wang, H., Cai, Z., and Zhang, L.: Impact of 3DVAR assimilation of surface PM2.5 observations on PM2.5 forecasts over China during wintertime, *Atmos. Environ.*, 187, 34-49, 10.1016/j.atmosenv.2018.05.049, 2018.
- 675 Fu, W. and Zhu, J.: Effects of Sea Level Data Assimilation by Ensemble Optimal Interpolation and 3D Variational Data Assimilation on the Simulation of Variability in a Tropical Pacific Model, *Journal of Atmospheric and Oceanic Technology*, 28, 1624-1640, 10.1175/jtech-d-11-00044.1, 2011.
- Gandin, L. S.: *Objective Analysis of Meteorological Fields*, 1963.
- Ghorani-Azam, A., Riahi-Zanjani, B., and Balali-Mood, M.: Effects of air pollution on human health and practical measures for prevention in Iran, *J. Res. Med. Sci.*, 21, 65, 10.4103/1735-1995.189646, 2016.
- 680 Gilchrist, B. and Cressman, G. P.: An Experiment in Objective Analysis, *Tellus*, 6, 309-318, 10.3402/tellusa.v6i4.8762, 1954.
- Gong, S. L. and Zhang, X. Y.: CUACE/Dust &ndash; an integrated system of observation and modeling systems for operational dust forecasting in Asia, *Atmos. Chem. Phys.*, 8, 2333-2340, 10.5194/acp-8-2333-2008, 2008.
- Kalman, R. E.: A New Approach to Linear Filtering and Prediction Problems, *Journal of Basic Engineering*, 82, 35-45, 10.1115/1.3662552, 1960.
- 685 Lee, L. A., Reddington, C. L., and Carslaw, K. S.: On the relationship between aerosol model uncertainty and radiative forcing uncertainty, *Proc Natl Acad Sci U S A*, 113, 5820-5827, 10.1073/pnas.1507050113, 2016.
- Li, Z., Zang, Z., Li, Q. B., Chao, Y., Chen, D., Ye, Z., Liu, Y., and Liou, K. N.: A three-dimensional variational data assimilation system for multiple aerosol species with WRF/Chem and an application to PM<sub>2.5</sub> prediction, *Atmos. Chem. Phys.*, 13, 4265-4278, 10.5194/acp-13-4265-2013, 2013.
- 690 Lin, C., Wang, Z., and J, Z.: A data assimilation method of the Ensemble Kalman Filter for use in severe dust storm forecasts over China, *Atmospheric Chemistry and Physics Discussions*, 7, 10.5194/acpd-7-17511-2007, 2007.
- Liu, C., Zhang, S., Gao, Y., Wang, Y., Sheng, L., Gao, H., and Fung, J. C. H.: Optimal estimation of initial concentrations and emission sources with 4D-Var for air pollution prediction in a 2D transport model, *Sci Total Environ*, 773, 145580, 10.1016/j.scitotenv.2021.145580, 2021.
- 695 Liu, F., Tan, Q., Jiang, X., Yang, F., and Jiang, W.: Effects of relative humidity and PM2.5 chemical compositions on visibility impairment in Chengdu, China, *Journal of Environmental Sciences*, 86, 15-23, <https://doi.org/10.1016/j.jes.2019.05.004>, 2019.

- Liu, Z., Liu, Q., Lin, H.-C., Schwartz, C. S., Lee, Y.-H., and Wang, T.: Three-dimensional variational assimilation of MODIS aerosol optical depth: Implementation and application to a dust storm over East Asia, *Journal of Geophysical Research: Atmospheres*, 116, <https://doi.org/10.1029/2011JD016159>, 2011.
- 700 Lopez-Restrepo, S., Yarce, A., Pinel, N., Quintero, O. L., Segers, A., and Heemink, A. W.: Forecasting PM10 and PM2.5 in the Aburrá Valley (Medellín, Colombia) via EnKF based data assimilation, *Atmos. Environ.*, 232, 10.1016/j.atmosenv.2020.117507, 2020.
- Mauricio Agudelo, O., Viaene, P., and De Moor, B.: Improving the PM10 estimates of the air quality model AURORA by using Optimal Interpolation\*\*This work was supported by: • Research Council KUL: CoE PFV/10/002 (OPTEC), PhD/Postdoc grants • Flemish Government: iMinds Medical Information Technologies SBO 2015 • Belgian Federal Science Policy Office: IUAP P7/19 (DYSCO, 705 Dynamical systems, control and optimization, 2012-2017), IFAC-PapersOnLine, 48, 1154-1159, <https://doi.org/10.1016/j.ifacol.2015.12.287>, 2015.
- Natvik, L. J. and Evensen, G.: Assimilation of ocean colour data into a biochemical model of the North Atlantic: Part 1. Data assimilation experiments, *Journal of Marine Systems*, 40-41, 127-153, [https://doi.org/10.1016/S0924-7963\(03\)00016-2](https://doi.org/10.1016/S0924-7963(03)00016-2), 2003.
- Navon, I. M.: Data Assimilation for Numerical Weather Prediction: A Review, in: *Data Assimilation for Atmospheric, Oceanic and Hydrologic Applications*, edited by: Park, S. K., and Xu, L., Springer Berlin Heidelberg, Berlin, Heidelberg, 21-65, 10.1007/978-3-540-71056-1\_2, 2009.
- 710 Oke, P., Brassington, G., Griffin, D., and Schiller, A.: Ocean Data Assimilation: a case for ensemble optimal interpolation, *Australian Meteorological and Oceanographic Journal*, 59, 10.22499/2.5901.008, 2010.
- Oke, P. R., Sakov, P., and Corney, S. P.: Impacts of localisation in the EnKF and EnOI: experiments with a small model, *Ocean Dynamics*, 715 57, 32-45, 10.1007/s10236-006-0088-8, 2007.
- Oke, P. R., Allen, J. S., Miller, R. N., Egbert, G. D., and Kosro, P. M.: Assimilation of surface velocity data into a primitive equation coastal ocean model, *Journal of Geophysical Research: Oceans*, 107, 5-1-5-25, <https://doi.org/10.1029/2000JC000511>, 2002.
- Pagowski, M. and Grell, G. A.: Experiments with the assimilation of fine aerosols using an ensemble Kalman filter, *Journal of Geophysical Research: Atmospheres*, 117, <https://doi.org/10.1029/2012JD018333>, 2012.
- 720 Panofsky, R. A.: OBJECTIVE WEATHER-MAP ANALYSIS, *Journal of Atmospheric Sciences*, 6, 386-392, 10.1175/1520-0469(1949)006<0386:Owma>2.0.Co;2, 1949.
- Park, S. Y., Dash, U. K., Yu, J., Yumimoto, K., Uno, I., and Song, C. H.: Implementation of an ensemble Kalman filter in the Community Multiscale Air Quality model (CMAQ model v5.1) for data assimilation of ground-level PM2.5, *Geosci. Model Dev.*, 15, 2773-2790, 10.5194/gmd-15-2773-2022, 2022.
- 725 Peng, X., Xiao, F., Ohfuchi, W., and Fuchigami, H.: Conservative Semi-Lagrangian Transport on a Sphere and the Impact on Vapor Advection in an Atmospheric General Circulation Model, *Monthly Weather Review*, 133, 504-520, 10.1175/mwr-2869.1, 2005.
- Peng, Y., Wang, H., Hou, M., Jiang, T., Zhang, M., Zhao, T., and Che, H.: Improved method of visibility parameterization focusing on high humidity and aerosol concentrations during fog-haze events: Application in the GRAPES\_CAUCE model in Jing-Jin-Ji, China, *Atmospheric Environment*, 222, 117139, <https://doi.org/10.1016/j.atmosenv.2019.117139>, 2020.
- 730 Peng, Y., Wang, H., Zhang, X., Zhao, T., Jiang, T., Che, H., Zhang, X., Zhang, W., and Liu, Z.: Impacts of PBL schemes on PM2.5 simulation and their responses to aerosol-radiation feedback in GRAPES\_CUACE model during severe haze episodes in Jing-Jin-Ji, China, *Atmospheric Research*, 248, 105268, <https://doi.org/10.1016/j.atmosres.2020.105268>, 2021a.
- Peng, Y., Wang, H., Zhang, X., Zhao, T., Jiang, T., Che, H., Zhang, X., Zhang, W., and Liu, Z.: Impacts of PBL schemes on PM2.5 simulation and their responses to aerosol-radiation feedback in GRAPES\_CUACE model during severe haze episodes in Jing-Jin-Ji, China, 735 *Atmospheric Research*, 248, 10.1016/j.atmosres.2020.105268, 2021b.
- Peng, Z., Liu, Z., Chen, D., and Ban, J.: Improving PM2.5 forecast over China by the joint adjustment of initial conditions and source emissions with an ensemble Kalman filter, *Atmos. Chem. Phys.*, 17, 4837-4855, 10.5194/acp-17-4837-2017, 2017.
- Perez, P., Menares, C., and Ramirez, C.: PM2.5 forecasting in Coyhaique, the most polluted city in the Americas, *Urban. Clim.*, 32, 10.1016/j.uclim.2020.100608, 2020.
- 740 Piovani, C.: The “Greening” of China: Progress, Limitations, and Contradictions, *Journal of Contemporary Asia*, 47, 93-115, 10.1080/00472336.2016.1203011, 2017.
- Sahu, S. K. and Kota, S. H.: Significance of PM2.5 Air Quality at the Indian Capital, *Aerosol and Air Quality Research*, 17, 588-597, 10.4209/aaqr.2016.06.0262, 2017.
- 745 Skachko, S., Ménard, R., Errera, Q., Christophe, Y., and Chabrilat, S.: EnKF and 4D-Var data assimilation with chemical transport model BASCOE (version 05.06), *Geosci. Model Dev.*, 9, 2893-2908, 10.5194/gmd-9-2893-2016, 2016.
- Talagrand, O. and Courtier, P.: Variational Assimilation of Meteorological Observations With the Adjoint Vorticity Equation. I: Theory, *Q. J. R. Meteorol. Soc.*, 113, 1311-1328, <https://doi.org/10.1002/qj.49711347812>, 1987.
- Tang, X., Zhu, J., Wang, Z. F., and Gbaguidi, A.: Improvement of ozone forecast over Beijing based on ensemble Kalman filter with simultaneous adjustment of initial conditions and emissions, *Atmos. Chem. Phys.*, 11, 12901-12916, 10.5194/acp-11-12901-2011, 2011.
- 750 Tang, X., Zhu, J., Wang, Z., Gbaguidi, A., Lin, C., Xin, J., Song, T., and Hu, B.: Limitations of ozone data assimilation with adjustment of NOx emissions: mixed effects on NO2 forecasts over Beijing and surrounding areas, *Atmos. Chem. Phys.*, 16, 6395-6405, 10.5194/acp-16-6395-2016, 2016.

- 755 Tang, Y., Chai, T., Pan, L., Lee, P., Tong, D., Kim, H.-C., and Chen, W.: Using optimal interpolation to assimilate surface measurements and satellite AOD for ozone and PM<sub>2.5</sub>: A case study for July 2011, *Journal of the Air & Waste Management Association*, 65, 1206-1216, 10.1080/10962247.2015.1062439, 2015.
- Ting, Y.-C., Young, L.-H., Lin, T.-H., Tsay, S.-C., Chang, K.-E., and Hsiao, T.-C.: Quantifying the impacts of PM<sub>2.5</sub> constituents and relative humidity on visibility impairment in a suburban area of eastern Asia using long-term in-situ measurements, *Science of The Total Environment*, 818, 151759, <https://doi.org/10.1016/j.scitotenv.2021.151759>, 2022.
- 760 Tombette, M., Mallet, V., and Sportisse, B.: PM<sub>10</sub> data assimilation over Europe with the optimal interpolation method, *Atmos. Chem. Phys.*, 9, 57-70, 10.5194/acp-9-57-2009, 2009.
- Wang, C., An, X., Hou, Q., Sun, Z., Li, Y., and Li, J.: Development of four-dimensional variational assimilation system based on the GRAPES-CUACE adjoint model (GRAPES-CUACE-4D-Var V1.0) and its application in emission inversion, *Geosci. Model Dev.*, 14, 337-350, 10.5194/gmd-14-337-2021, 2021.
- 765 Wang, D., You, W., Zang, Z., Pan, X., He, H., and Liang, Y.: A three-dimensional variational data assimilation system for a size-resolved aerosol model: Implementation and application for particulate matter and gaseous pollutant forecasts across China, *Science China Earth Sciences*, 63, 1366-1380, 10.1007/s11430-019-9601-4, 2020.
- Wang, H. and Niu, T.: Sensitivity studies of aerosol data assimilation and direct radiative feedbacks in modeling dust aerosols, *Atmos. Environ.*, 64, 208-218, 10.1016/j.atmosenv.2012.09.066, 2013.
- 770 Wang, H., Zhang, X., Gong, S., Chen, Y., Shi, G., and Li, W.: Radiative feedback of dust aerosols on the East Asian dust storms, *Journal of Geophysical Research: Atmospheres*, 115, <https://doi.org/10.1029/2009JD013430>, 2010a.
- Wang, H., Peng, Y., Zhang, X., Liu, H., Zhang, M., Che, H., Cheng, Y., and Zheng, Y.: Contributions to the explosive growth of PM<sub>2.5</sub> mass due to aerosol-radiation feedback and decrease in turbulent diffusion during a red alert heavy haze in Beijing-Tianjin-Hebei, China, *Atmos. Chem. Phys.*, 18, 17717-17733, 10.5194/acp-18-17717-2018, 2018.
- 775 Wang, H., Xue, M., Zhang, X. Y., Liu, H. L., Zhou, C. H., Tan, S. C., Che, H. Z., Chen, B., and Li, T.: Mesoscale modeling study of the interactions between aerosols and PBL meteorology during a haze episode in Jing-Jin-Ji (China) and its nearby surrounding region - Part 1: Aerosol distributions and meteorological features, *Atmospheric Chemistry & Physics*, 15, 3257, 10.5194/acp-15-3257-2015, 2015.
- Wang, H., Gong, S., Zhang, H., Chen, Y., Shen, X., Chen, D., Xue, J., Shen, Y., Wu, X., and Jin, Z.: A new-generation sand and dust storm forecasting system GRAPES-CUACE/Dust: Model development, verification and numerical simulation, *Chinese Science Bulletin*, 55, 635-649, 10.1007/s11434-009-0481-z, 2010b.
- 780 Wang, P., Wang, H., Wang, Y. Q., Zhang, X. Y., Gong, S. L., Xue, M., Zhou, C. H., Liu, H. L., An, X. Q., Niu, T., and Cheng, Y. L.: Inverse modeling of black carbon emissions over China using ensemble data assimilation, *Atmos. Chem. Phys.*, 16, 989-1002, 10.5194/acp-16-989-2016, 2016.
- Wang, Y. Q., Zhang, X. Y., Gong, S. L., Zhou, C. H., Hu, X. Q., Liu, H. L., Niu, T., and Yang, Y. Q.: Surface observation of sand and dust storm in East Asia and its application in CUACE/Dust, *Atmos. Chem. Phys.*, 8, 545-553, 10.5194/acp-8-545-2008, 2008.
- 785 Xiao, Q., Geng, G., Liang, F., Wang, X., Lv, Z., Lei, Y., Huang, X., Zhang, Q., Liu, Y., and He, K.: Changes in spatial patterns of PM<sub>2.5</sub> pollution in China 2000-2018: Impact of clean air policies, *Environ. Int.*, 141, 105776, 10.1016/j.envint.2020.105776, 2020.
- Xie, J. and Zhu, J.: Ensemble optimal interpolation schemes for assimilating Argo profiles into a hybrid coordinate ocean model, *Ocean Model.*, 33, 283-298, 10.1016/j.ocemod.2010.03.002, 2010.
- 790 Yadav, R., Sugha, A., Bhatti, M. S., Kansal, S. K., Sharma, S. K., and Mandal, T. K.: The role of particulate matter in reduced visibility and anionic composition of winter fog: a case study for Amritsar city, *RSC Advances*, 12, 11104-11112, 10.1039/D2RA00424K, 2022.
- Ye, H., Pan, X., You, W., Zhu, X., Zang, Z., Wang, D., Zhang, X., Hu, Y., and Jin, S.: Impact of CALIPSO profile data assimilation on 3-D aerosol improvement in a size-resolved aerosol model, *Atmospheric Research*, 264, 105877, <https://doi.org/10.1016/j.atmosres.2021.105877>, 2021.
- 795 Yu, X., Ma, J., An, J., Yuan, L., Zhu, B., Liu, D., Wang, J., Yang, Y., and Cui, H.: Impacts of meteorological condition and aerosol chemical compositions on visibility impairment in Nanjing, China, *Journal of Cleaner Production*, 131, 112-120, <https://doi.org/10.1016/j.jclepro.2016.05.067>, 2016.
- Zhai, S., An, X., Zhao, T., Sun, Z., Wang, W., Hou, Q., Guo, Z., and Wang, C.: Detection of critical PM<sub>2.5</sub> emission sources and their contributions to a heavy haze episode in Beijing, China, using an adjoint model, *Atmos. Chem. Phys.*, 18, 6241-6258, 10.5194/acp-18-6241-2018, 2018.
- 800 Zhang, F., Zhang, M., Huang, X.-Y., and Zhang, X.: Intercomparison of an Ensemble Kalman Filter with Three- and Four-Dimensional Variational Data Assimilation Methods in a Limited-Area Model over the Month of June 2003, *Mon. Weather Rev.*, 139, 566-572, 10.1175/2010mwr3610.1, 2011.
- Zhang, R., Jing, J., Tao, J., Hsu, S. C., Wang, G., Cao, J., Lee, C. S. L., Zhu, L., Chen, Z., Zhao, Y., and Shen, Z.: Chemical characterization and source apportionment of PM<sub>2.5</sub> in Beijing: seasonal perspective, *Atmos. Chem. Phys.*, 13, 7053-7074, 10.5194/acp-13-7053-2013, 2013.
- 805 Zhang, W., Zhang, X., and Wang, H.: The Role of Aerosol-Radiation Interaction in the Meteorology Prediction at the Weather Scale in the Numerical Weather Prediction Model, *Geophysical Research Letters*, 49, e2021GL097026, <https://doi.org/10.1029/2021GL097026>, 2022.

- 810 Zheng, B., Zhang, Q., Zhang, Y., He, K. B., Wang, K., Zheng, G. J., Duan, F. K., Ma, Y. L., and Kimoto, T.: Heterogeneous chemistry: a mechanism missing in current models to explain secondary inorganic aerosol formation during the January 2013 haze episode in North China, *Atmos. Chem. Phys.*, 15, 2031-2049, 10.5194/acp-15-2031-2015, 2015.
- Zheng, H., Liu, J., Tang, X., Wang, Z., Wu, H., Yan, P., and Wang, W.: Improvement of the Real-time PM<sub>2.5</sub> Forecast over the Beijing-Tianjin-Hebei Region using an Optimal Interpolation Data Assimilation Method, *Aerosol Air Qual. Res.*, 18, 1305-1316, 10.4209/aaqr.2017.11.0522, 2018.
- 815 Zhou, C.-H., Gong, S., Zhang, X.-Y., Liu, H.-L., Xue, M., Cao, G.-L., An, X.-Q., Che, H.-Z., Zhang, Y.-M., and Niu, T.: Towards the improvements of simulating the chemical and optical properties of Chinese aerosols using an online coupled model – CUACE/Aero, *Tellus B: Chemical and Physical Meteorology*, 64, 18965, 10.3402/tellusb.v64i0.18965, 2012.

820



**Table1. Mass concentration limit of PM<sub>2.5</sub> and its corresponding air quality level and air pollution index (API)**

<u>PM<sub>2.5</sub> concentration</u> <u>limit (ug m<sup>-3</sup>)</u>	<u>Air quality description</u>	<u>level</u>	<u>API</u>
<u>35</u>	<u>excellent</u>	<u>I</u>	<u>0-50</u>
<u>75</u>	<u>good</u>	<u>II</u>	<u>51-100</u>
<u>115</u>	<u>light pollution</u>	<u>III</u>	<u>101-150</u>
<u>150</u>	<u>moderate pollution</u>	<u>IV</u>	<u>151-200</u>
<u>250</u>	<u>heavy pollution</u>	<u>V</u>	<u>201-300</u>
<u>&gt;250</u>	<u>hazardous pollution</u>	<u>VI</u>	<u>&gt;300</u>

825

**Table24. Experimental design.**

<b>Name</b>	<b>Experiment</b>	<b>Design</b>
<b>Control experiment</b>	CR00	Warm restart (WS) at 0000 UTC and without DA
	CR12	WS at 1200 UTC and without DA
<b>Sensitivity experiment</b>	L20km N48 WS00	Fixed ensemble size N of 48, assimilation of the initial field at 0000 UTC per day, and localization length scale L of 20, 40, 60, 80, 100 km were selected for the assimilation experiment
	L40km N48 WS00	
	L60km N48 WS00	
	L80km N48 WS00	
	L100km N48 WS00	
	L80km N24 WS 00	Fixed localization length scale L of 80 km, assimilation of the initial field at 0000 UTC per day, and ensemble size N of 24, 48, 72, 96, 120, 144 km were selected for the assimilation experiment
	L80km N48 WS 00	
	L80km N72 WS 00	
L80km N96 WS 00	Fixed localization length scale L of 80 km, assimilation of the initial field at 0000 UTC per day, and ensemble size N of 24, 48, 72, 96, 120, 144 km were selected for the assimilation experiment	
L80km N120 WS 00		
L80km N144 WS 00		
	DA00	WS at 0000 UTC and with DA

	DA12	WS at 1200 UTC and with DA
<u>Name</u>	<u>Experiment</u>	<u>Design</u>
<u>Control experiment</u>	<u>CR00</u>	<u>Model control run without DA begin at 0000 UTC every day and forecast 24 hours</u>
	<u>CR12</u>	<u>Model control run without DA begin at 1200 UTC every day and forecast 24 hours</u>
<u>Sensitivity experiment</u>	<u>Lxxkm-N48</u>	<u>assimilation at 0000 UTC with fixed ensemble size N of 48 and different localization length-scale Lxx of 20, 40, 60, 80, 100 km</u>
	<u>L80km-Nyy</u>	<u>assimilation at 0000 UTC with fixed localization length-scale L of 80 km and different ensemble size Nyy of 24, 48, 72, 96, 120, 144</u>
<u>Cycling assimilation experiment</u>	<u>DA00</u>	<u>Model forecast with assimilation at 0000 UTC every day</u>
	<u>DA12</u>	<u>Model forecast with assimilation at 1200 UTC every day</u>
	<u>DA00&amp;12</u>	<u>Model forecast with assimilation at 0000 UTC and 1200UTC everyday</u>
	<u>DA00&amp;12</u>	<u>Model forecast with assimilation at 0000 UTC and 1200UTC everyday</u>

**Table2. Statistics of the analysis fields PM<sub>2.5</sub> concentrations from 15 to 23 November 2016 at 0000 UTC for the sensitivity experiments with localization length-scale of 80km and ensemble size N of 24, 48, 72, 96, 120,144**

	<b>24</b>	<b>48</b>	<b>72</b>	<b>96</b>	<b>120</b>	<b>144</b>
<b>CORR</b>	0.970	0.974	0.975	0.975	0.959	0.961
<b>RMSE (ug m-3)</b>	20.675	19.170	18.908	18.849	23.919	23.416
<b>MB (ug m-3)</b>	2.160	1.963	1.943	1.938	2.514	2.560
<b>ME (ug m-3)</b>	12.061	11.158	10.943	10.858	13.997	13.532

830

**Table3. Statistics of PM<sub>2.5</sub> concentrations for verifications sites of the initial field without (CR) and with assimilation at 0000 UTC each day from 1 to 31 December 2016. Assimilation sensitivity experiments were performed with 48 ensemble samples and length-scale L of 20, 40, 60, 80, 100km respectively and only assimilated the assimilation sites.**

	<u>CORR</u>	<u>RMSE (<math>\mu\text{g m}^{-3}</math>)</u>	<u>MB (<math>\mu\text{g m}^{-3}</math>)</u>	<u>ME (<math>\mu\text{g m}^{-3}</math>)</u>
<u>CR</u>	<u>0.56</u>	<u>60.1</u>	<u>8.5</u>	<u>41.7</u>
<u>20</u>	<u>0.77</u>	<u>48.2</u>	<u>4.1</u>	<u>30.2</u>
<u>40</u>	<u>0.82</u>	<u>41.6</u>	<u>3.2</u>	<u>25.9</u>
<u>60</u>	<u>0.81</u>	<u>43.1</u>	<u>3.5</u>	<u>26.8</u>
<u>80</u>	<u>0.80</u>	<u>44.9</u>	<u>3.8</u>	<u>27.0</u>
<u>100</u>	<u>0.79</u>	<u>46.0</u>	<u>4.0</u>	<u>28.2</u>

**Table 3. Statistical comparison of PM<sub>2.5</sub> concentrations from the BFs and the assimilation experiment with 96 ensemble samples and a length scale of 40km (AFs) with all observations analyses by 0000UTC during the experiment period. The Total is China Mainland. The NC is North China.**

		<b>CORR</b>	<b>RMSE</b>	<b>MB</b>	<b>ME</b>
<b>Total</b>	<b>BF</b>	0.584	62.449	-0.416	41.578
	<b>AF</b>	0.967	17.280	2.137	10.174
	<i>f</i>	65.58%	-72.33%	-628.16%	-75.53%
<b>NC</b>	<b>BF</b>	0.391	98.639	-21.287	71.941
	<b>AF</b>	0.972	23.149	2.050	15.870
	<i>f</i>	148.59%	-75.53%	-109.63%	-79.59%

**Table 4. Statistics of PM<sub>2.5</sub> concentrations for verifications sites of the initial field without (CR) and with assimilation at 0000 UTC each day from 1 to 31 December 2016. Assimilation sensitivity experiments were performed with a localization length-scale L of 80 km and an ensemble size of 24, 48, 72, 96, 120, and 144, respectively and only assimilated the assimilation sites.**

	<b>CORR</b>	<b>RMSE (<math>\mu\text{g m}^{-3}</math>)</b>	<b>MB (<math>\mu\text{g m}^{-3}</math>)</b>	<b>ME (<math>\mu\text{g m}^{-3}</math>)</b>
<b>CR</b>	0.56	60.1	8.5	41.7
<b>24</b>	0.76	48.6	4.2	30.8
<b>48</b>	0.80	44.9	3.8	27.0
<b>72</b>	0.81	42.4	3.4	25.9
<b>96</b>	0.82	40.7	2.9	25.7
<b>120</b>	0.80	44.1	3.6	26.2
<b>144</b>	0.79	45.8	3.9	27.3

**Table5. Statistics of initial PM<sub>2.5</sub> concentrations for assimilation sites (DA) and verifications sites (Ve) before EnOI (BF) and after EnOI (AF) at 0000 UTC on 16, 19, 20 and 23 December 2016, respectively.**

<u>Date</u>	<u>site</u>	<u>IC</u>	<u>CORR</u>	<u>RMSE</u> <u>(<math>\mu\text{g m}^{-3}</math>)</u>	<u>ME</u> <u>(<math>\mu\text{g m}^{-3}</math>)</u>	<u>MB</u> <u>(<math>\mu\text{g m}^{-3}</math>)</u>
<u>16</u>	<u>DA</u>	<u>BF</u>	<u>0.50</u>	<u>50.8</u>	<u>9.1</u>	<u>38.2</u>
		<u>AF</u>	<u>0.98</u>	<u>11.0</u>	<u>0.9</u>	<u>7.1</u>
	<u>Ve</u>	<u>BF</u>	<u>0.48</u>	<u>56.5</u>	<u>9.7</u>	<u>42.8</u>
		<u>AF</u>	<u>0.73</u>	<u>39.1</u>	<u>2.5</u>	<u>25.2</u>
<u>19</u>	<u>Da</u>	<u>BF</u>	<u>0.65</u>	<u>81.5</u>	<u>-9.3</u>	<u>55.2</u>
		<u>AF</u>	<u>0.98</u>	<u>17.3</u>	<u>-1.2</u>	<u>10.4</u>
	<u>Ve</u>	<u>BF</u>	<u>0.66</u>	<u>79.2</u>	<u>-5.7</u>	<u>50.2</u>
		<u>AF</u>	<u>0.85</u>	<u>56.1</u>	<u>1.3</u>	<u>32.4</u>
<u>20</u>	<u>DA</u>	<u>BF</u>	<u>0.67</u>	<u>95.0</u>	<u>-24.2</u>	<u>64.5</u>
		<u>AF</u>	<u>0.99</u>	<u>19.1</u>	<u>-2.7</u>	<u>10.2</u>
	<u>Ve</u>	<u>BF</u>	<u>0.66</u>	<u>94.7</u>	<u>-20.5</u>	<u>60.5</u>
		<u>AF</u>	<u>0.87</u>	<u>60.2</u>	<u>-5.1</u>	<u>35.1</u>
<u>23</u>	<u>DA</u>	<u>BF</u>	<u>0.52</u>	<u>47.6</u>	<u>20.6</u>	<u>36.9</u>
		<u>AF</u>	<u>0.97</u>	<u>10.8</u>	<u>2.1</u>	<u>6.8</u>
	<u>Ve</u>	<u>BF</u>	<u>0.50</u>	<u>50.3</u>	<u>23.3</u>	<u>37.9</u>
		<u>AF</u>	<u>0.75</u>	<u>31.4</u>	<u>6.0</u>	<u>20.6</u>

Date	Site	IC	CORR	RMSE ( $\mu\text{g m}^{-3}$ )	MB ( $\mu\text{g m}^{-3}$ )	ME ( $\mu\text{g m}^{-3}$ )
16	DA	BF	0.50	50.8	9.1	38.2
		AF	0.98	11.0	0.9	7.1
	Ve	BF	0.48	56.5	9.7	42.8
		AF	0.73	39.1	2.5	25.2
19	DA	BF	0.65	81.5	-9.3	55.2
		AF	0.98	17.3	-1.2	10.4
	Ve	BF	0.66	79.2	-5.67	50.2
		AF	0.85	56.1	1.3	32.4
20	DA	BF	0.67	95.0	-24.2	64.5
		AF	0.99	19.1	-2.7	10.2
	Ve	BF	0.66	94.7	-20.5	60.5
		AF	0.87	60.2	-5.1	35.1
23	DA	BF	0.52	47.6	20.6	36.9
		AF	0.97	10.8	2.1	6.8
	Ve	BF	0.50	50.3	23.3	37.9
		AF	0.75	31.4	6.0	20.6

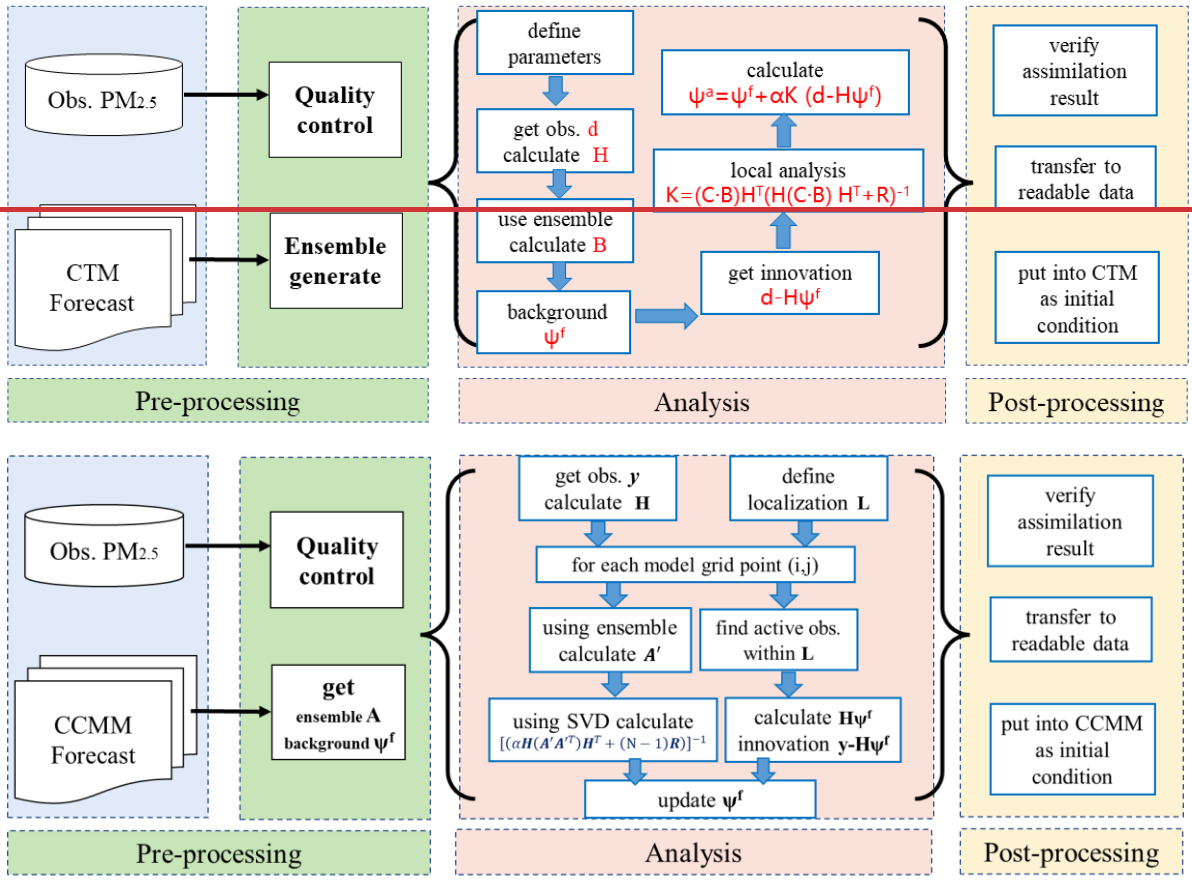
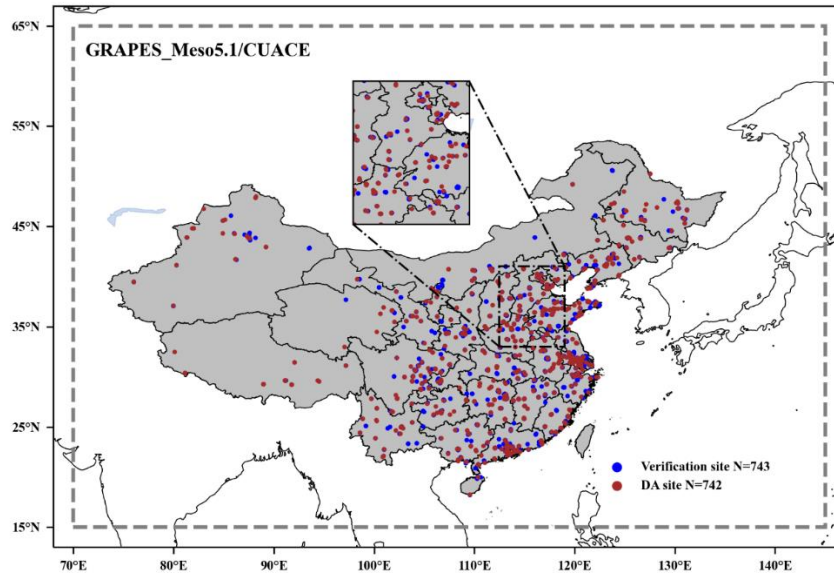


Figure 1. Flow chart of the main calculation procedures for EnOI initial field assimilation system. The Obs. PM<sub>2.5</sub> is ground-based observation of PM<sub>2.5</sub>. The CCMM is coupled chemistry meteorology model chemistry transport model. SVD is singular value decomposition



865 Figure 2. Simulation domain of GRAPES\_Meso5.1/CUACE. Minor region represents North China (NC). The locations of ground  
 stations in China mainland are marked on the maps with blue and brown dots. Only when the independence test is performed, the  
 brown assimilation sites and the blue verification sites are distinguished, otherwise, all sites are used as assimilation sites. The blue  
 and brown dots represent verification sites and assimilation sites, respectively. "N=743" means there are 743 verification sites.  
 "N=742" means there are 742 DA sites.

870



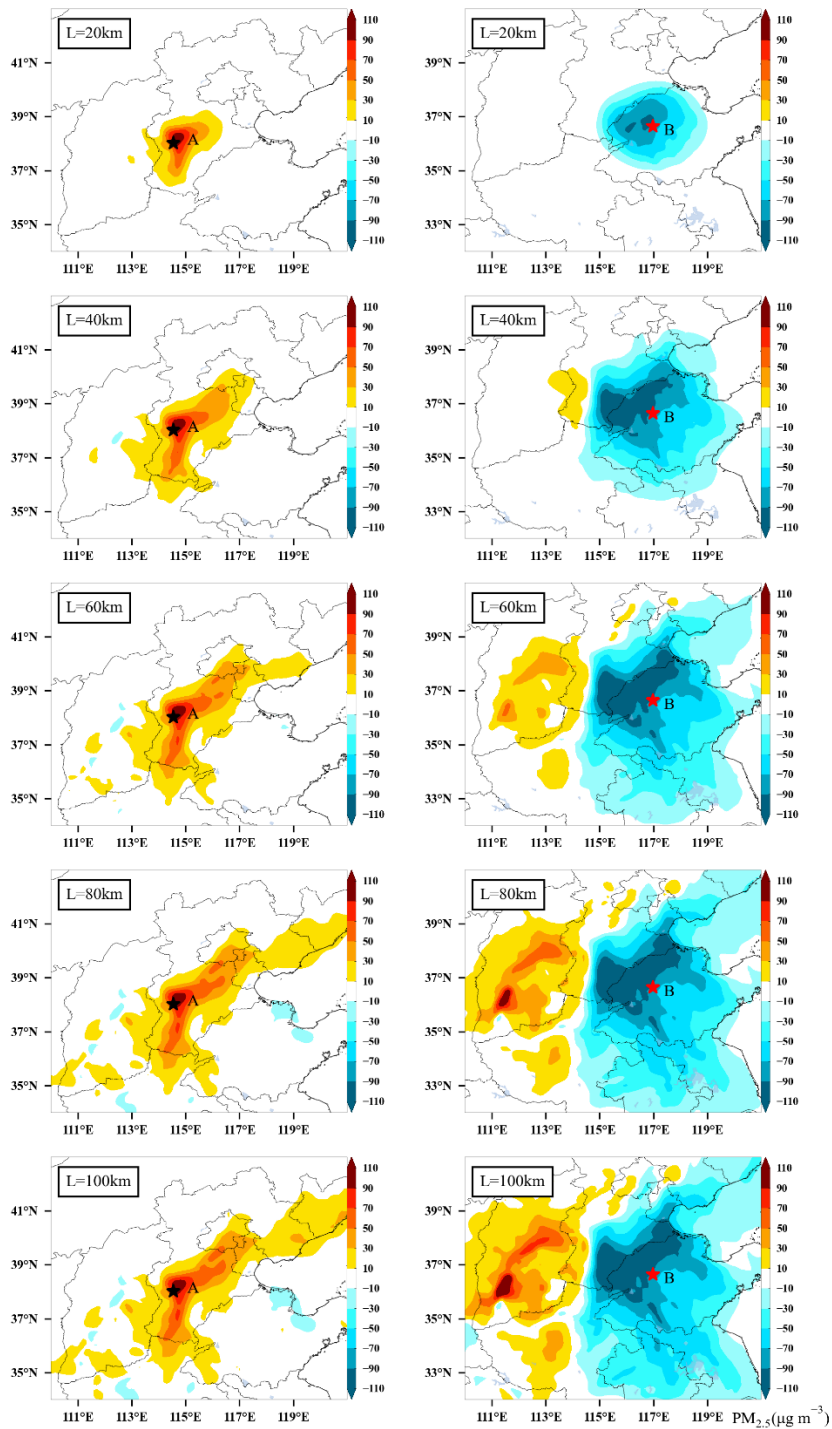
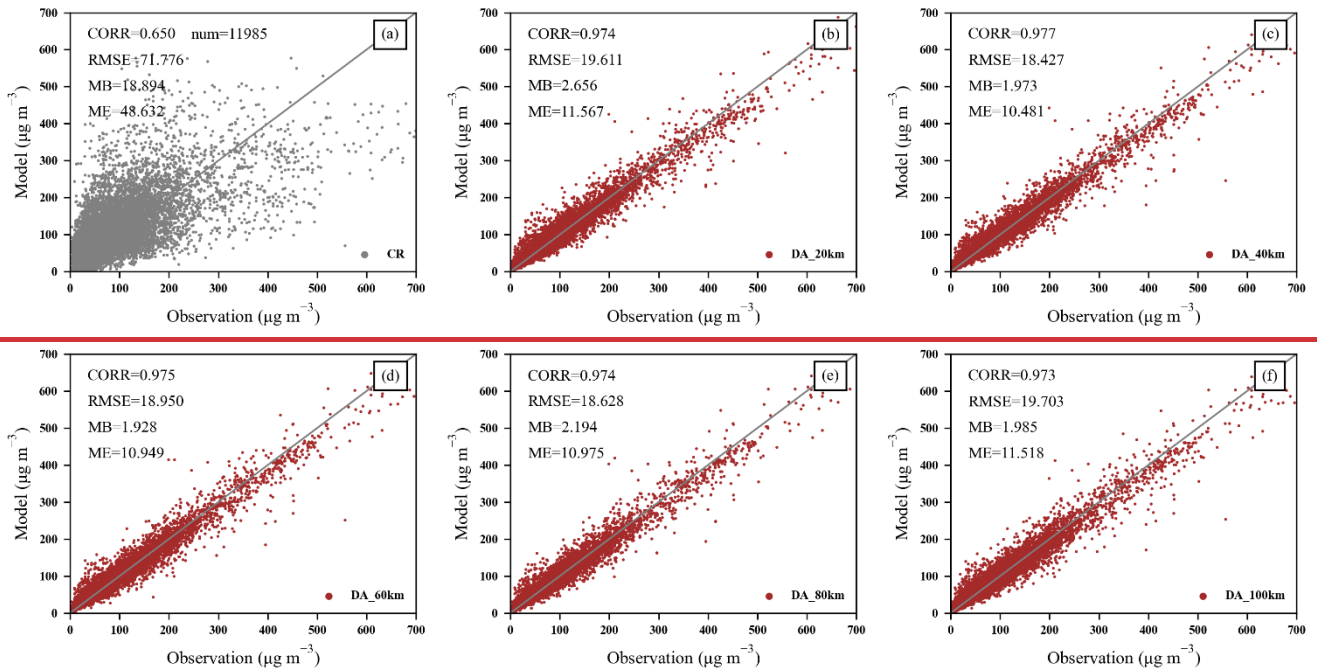
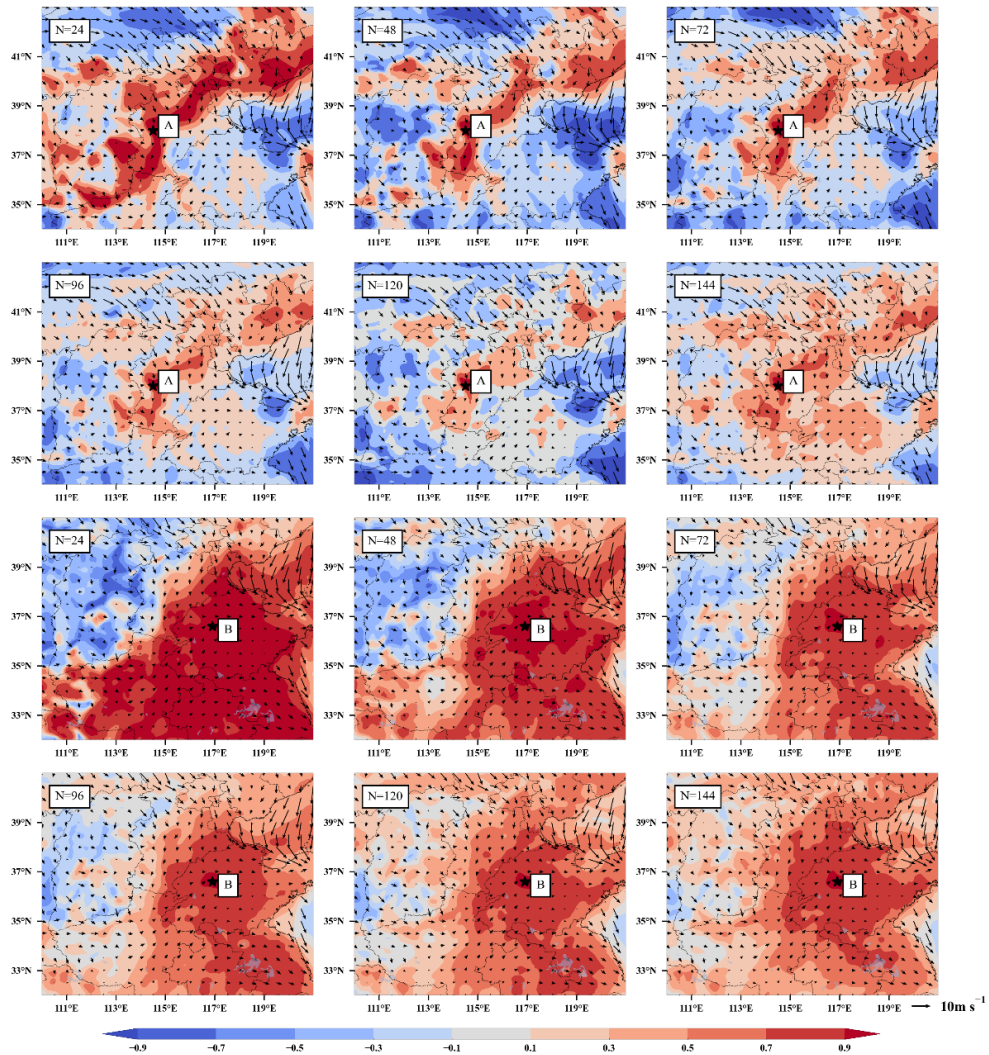


Figure 3. Spatial distribution of  $PM_{2.5}$  analysis increments after assimilation of initial fields at 0000 UTC on 15 December 2016, for assimilation site A ( $38.0^{\circ}$  N,  $114.5^{\circ}$  E) only (left column) and assimilation site B ( $36.6^{\circ}$  N,  $116.9^{\circ}$  E) only (right column) with fixed ensemble size 48 and different localization length-scale of 20, 40, 60, 80, 100km.



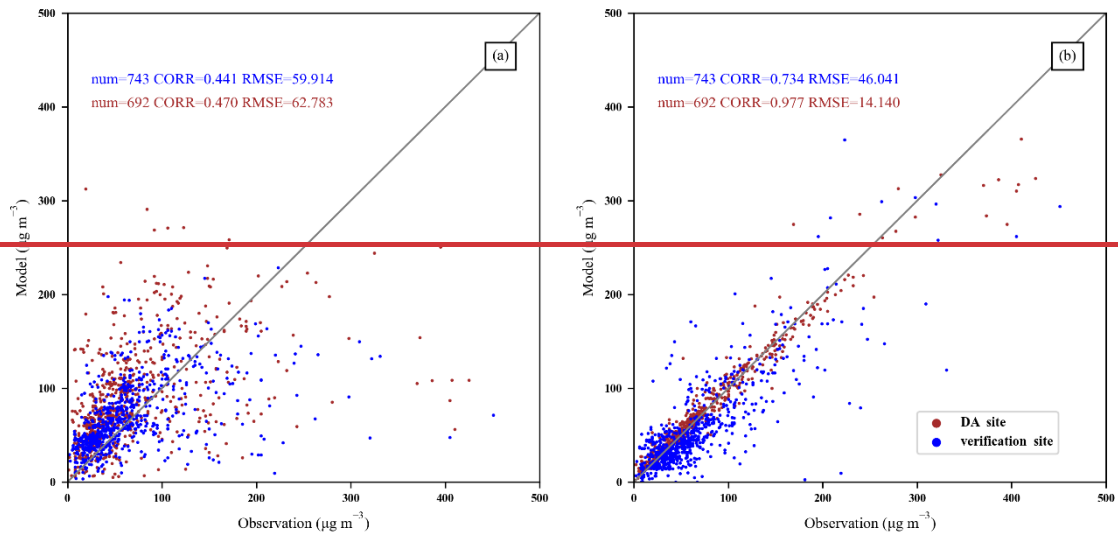
875

**Figure 4. Scatter plot of  $\text{PM}_{2.5}$  concentrations from the control experiment (CR) and the assimilation experiment with 40 ensemble samples and length-scale L of 20, 40, 60, 80, 100km (DA) with all observations analyses by 0000UTC during the experiment period. The num is the sum of all ground-based observations of  $\text{PM}_{2.5}$  stations during the experiment period.**



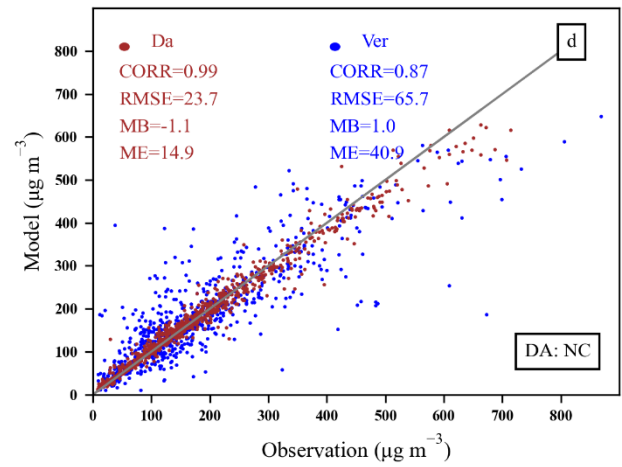
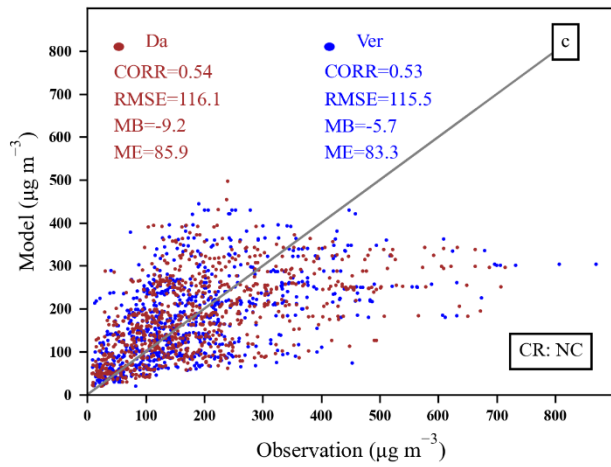
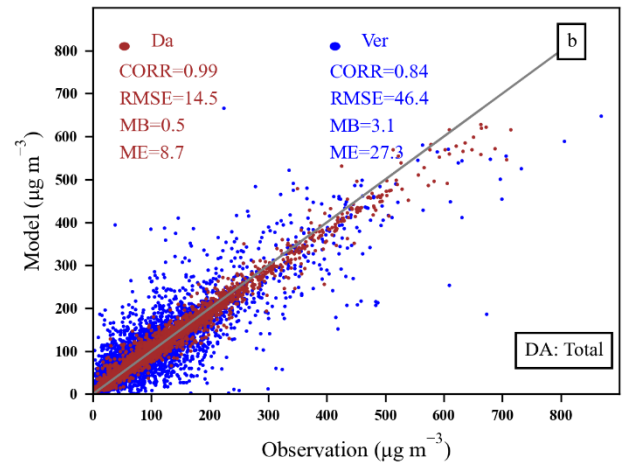
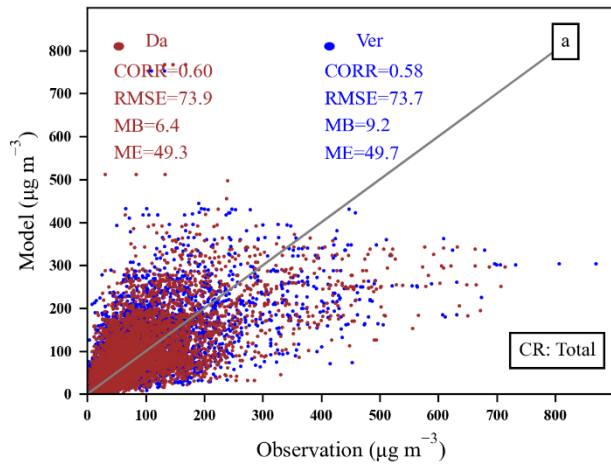
880

**Figure 54.** Spatial distribution of correlation coefficients of background error for site A ( $38.0^{\circ}$  N,  $114.5^{\circ}$  E) (rows 1, 2) and site B ( $36.6^{\circ}$  N,  $116.9^{\circ}$  E) (rows 3, 4) with ensemble error for assimilation experiments using length-scale of 80km and different ensemble size N of 24, 48, 72, 96, 120, 144 and wind vectors at 0000 UTC on 15 December 2016.

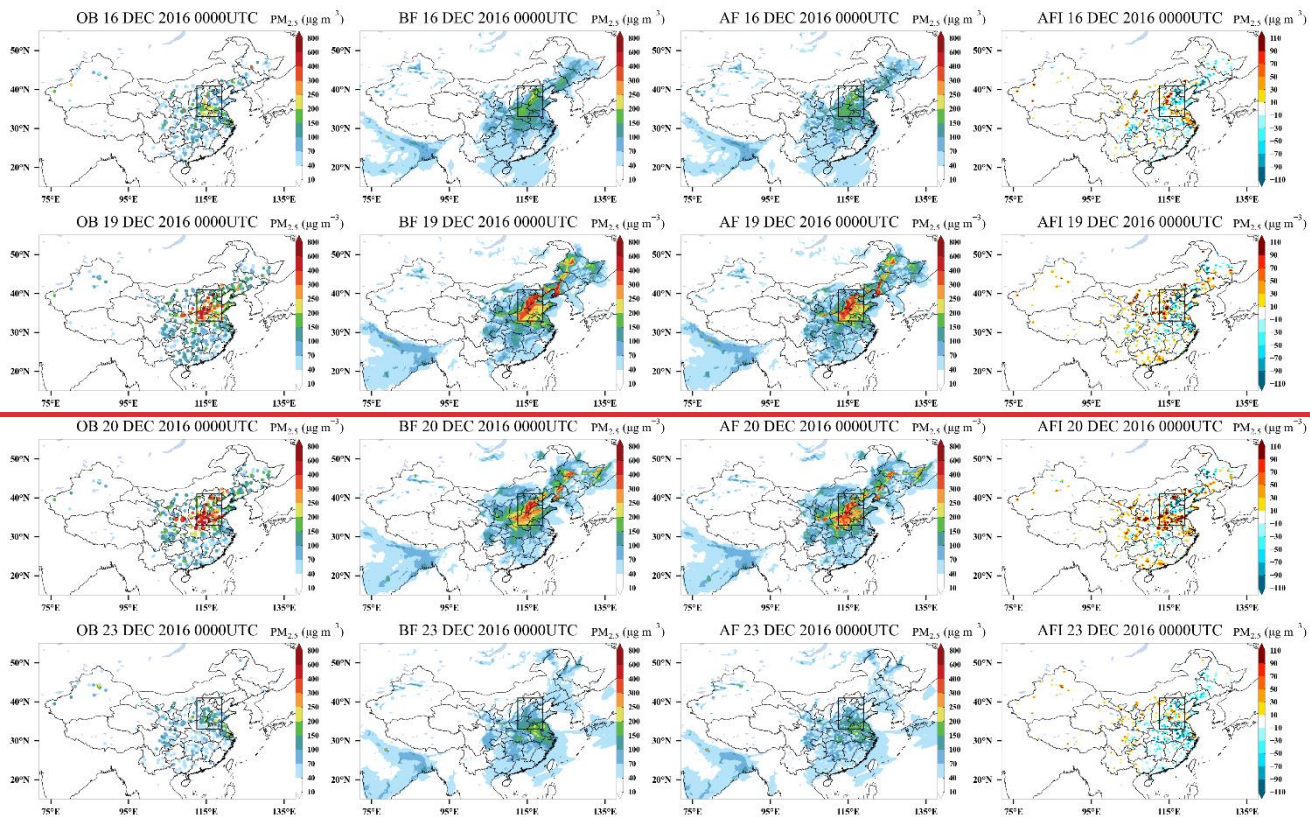


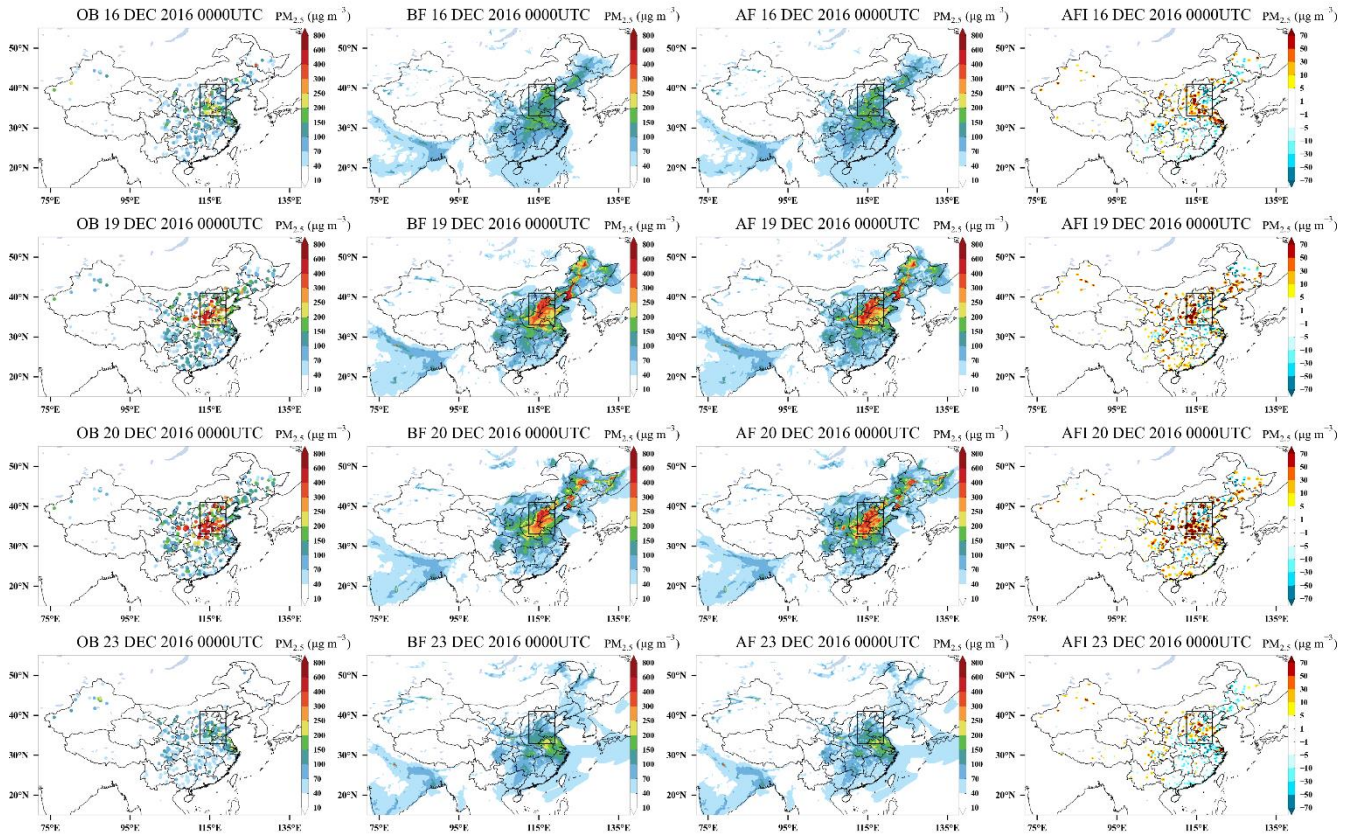
885

**Figure 6. Scatter plot of  $PM_{2.5}$  verification sites compared to assimilation (DA) sites for the control experiment (a) and assimilation experiment (b) using length-scale  $L=40\text{km}$  and ensemble size  $N=96$  at 0000UTC on 15 December 2016.**



**Figure 5. Scatter plot of PM<sub>2.5</sub> concentrations from the control experiment (a,c) and the assimilation experiment (b,d). The ensemble size in the assimilation experiment is 96 and the length-scale L is 40 km. Brown (Da) and blue (Ver) dots are assimilation sites and validation sites respectively. a, b is for mainland China (Total), c, d is for North China (NC).**





895 **Figure 76.** Snapshots of the horizontal distributions of PM<sub>2.5</sub> observation (OB), before (BF) and after (AF) the application of EnOI technique, analysis field increment (AFI) at 0000 UTC on 16, 19, 20, and 23, December 2016. The black box area, representing northernNorth China (NC), has the most serious PM<sub>2.5</sub> pollution.

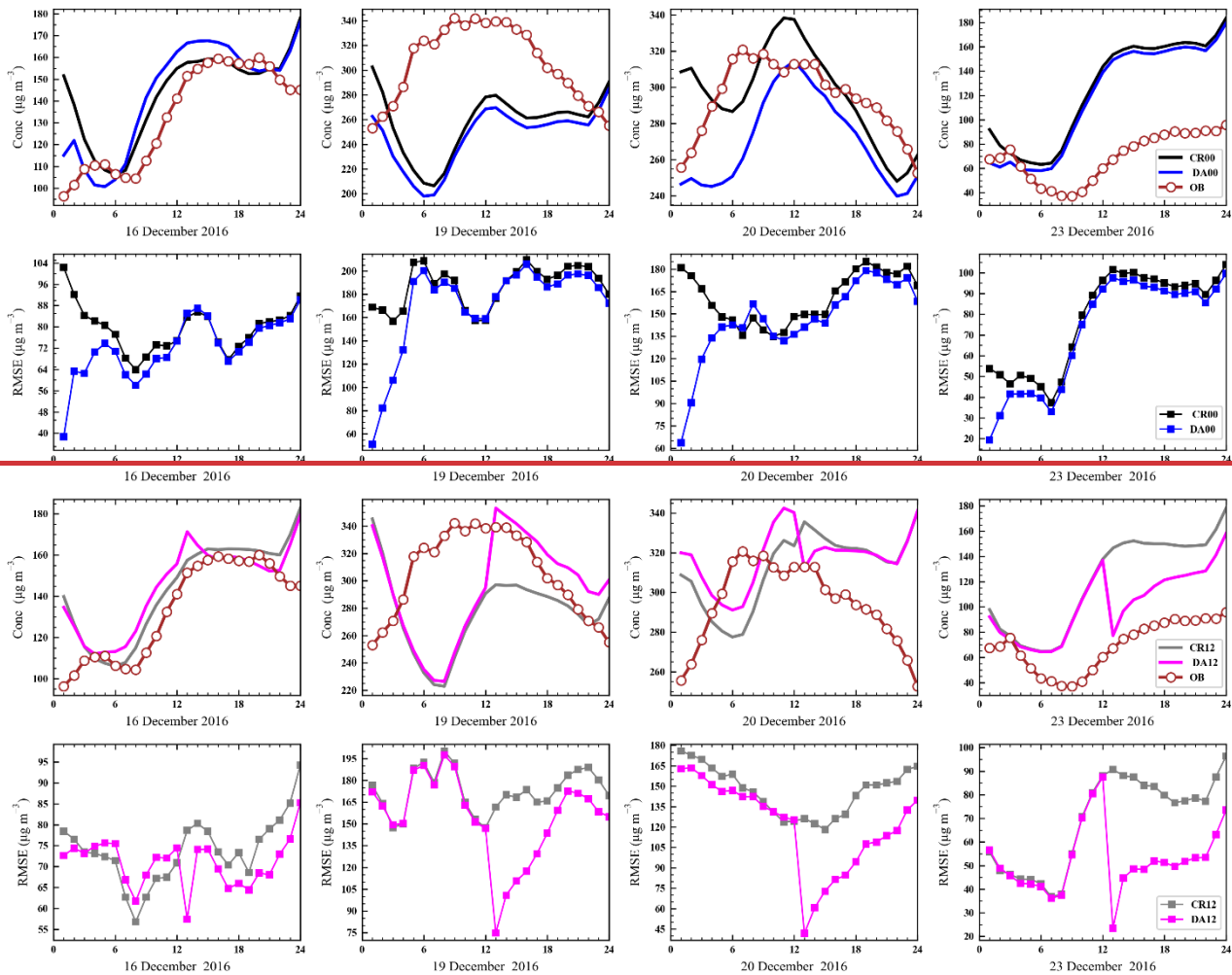


**Figure 8.** Mean forecasts and observations of  $PM_{2.5}$ , RMSE for North China, calculated against observations. x-axis refers to specific dates. The labels on the x-axis refer to the 24 hours of the day. DA00 and DA12 represent the initial field assimilation using EnOI at 0000 UTC and 1200 UTC each day, respectively. CR00 and CR12 are control experiments, representing warm restart without assimilation at 0000 UTC and 1200 UTC each day. The OB is hourly results of  $PM_{2.5}$  observations averaged over the North China region.



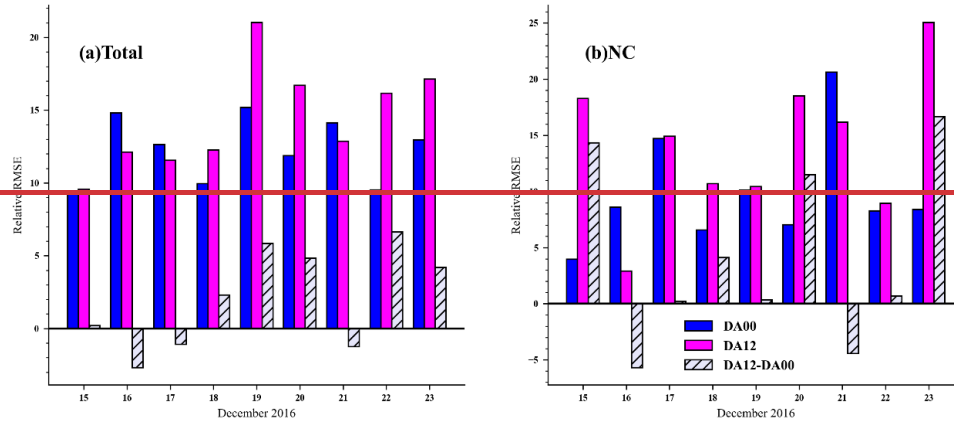
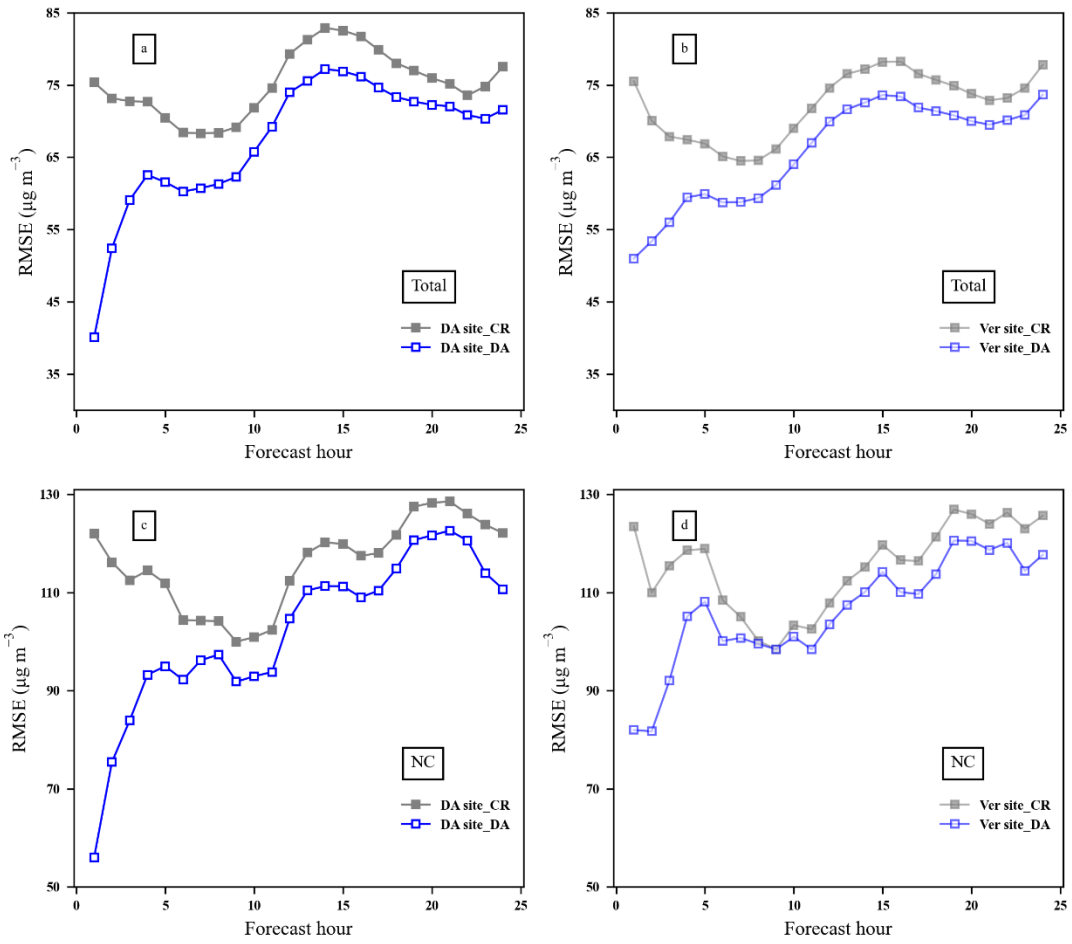


**Figure 9. Relative RMSE time series for 15 to 23 December 2016 for Mainland China (a), North China (b). The relative RMSE is calculated by the daily average RMSE.**



910 **Figure 7. The average RMSE value of surface PM<sub>2.5</sub> forecasts as a function of forecast time over (a) China Mainland for DA sites, (b) China Mainland for verification sites, (c) North China for DA sites, (d) North China for verification site.**

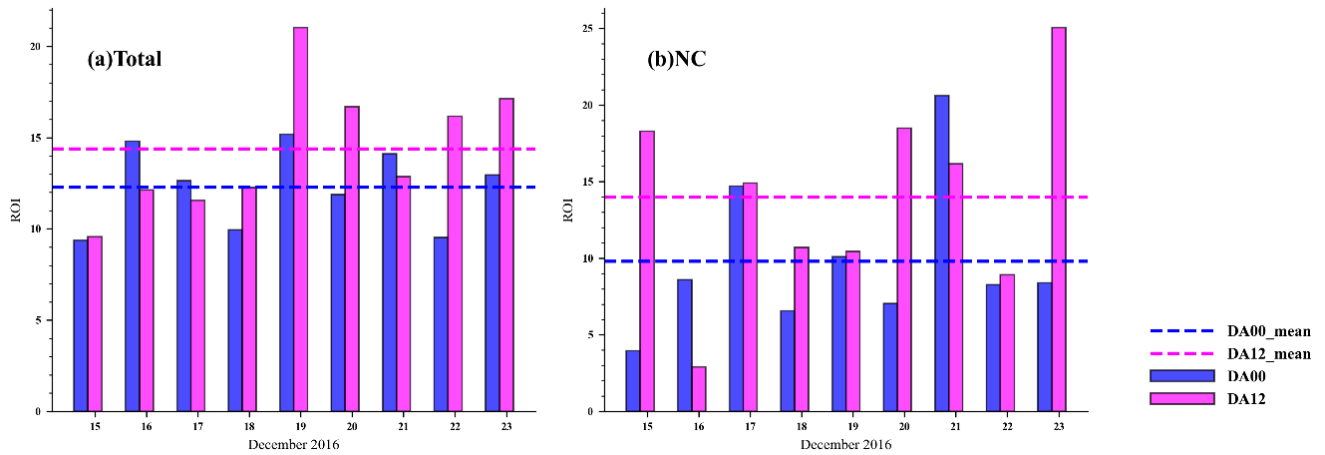
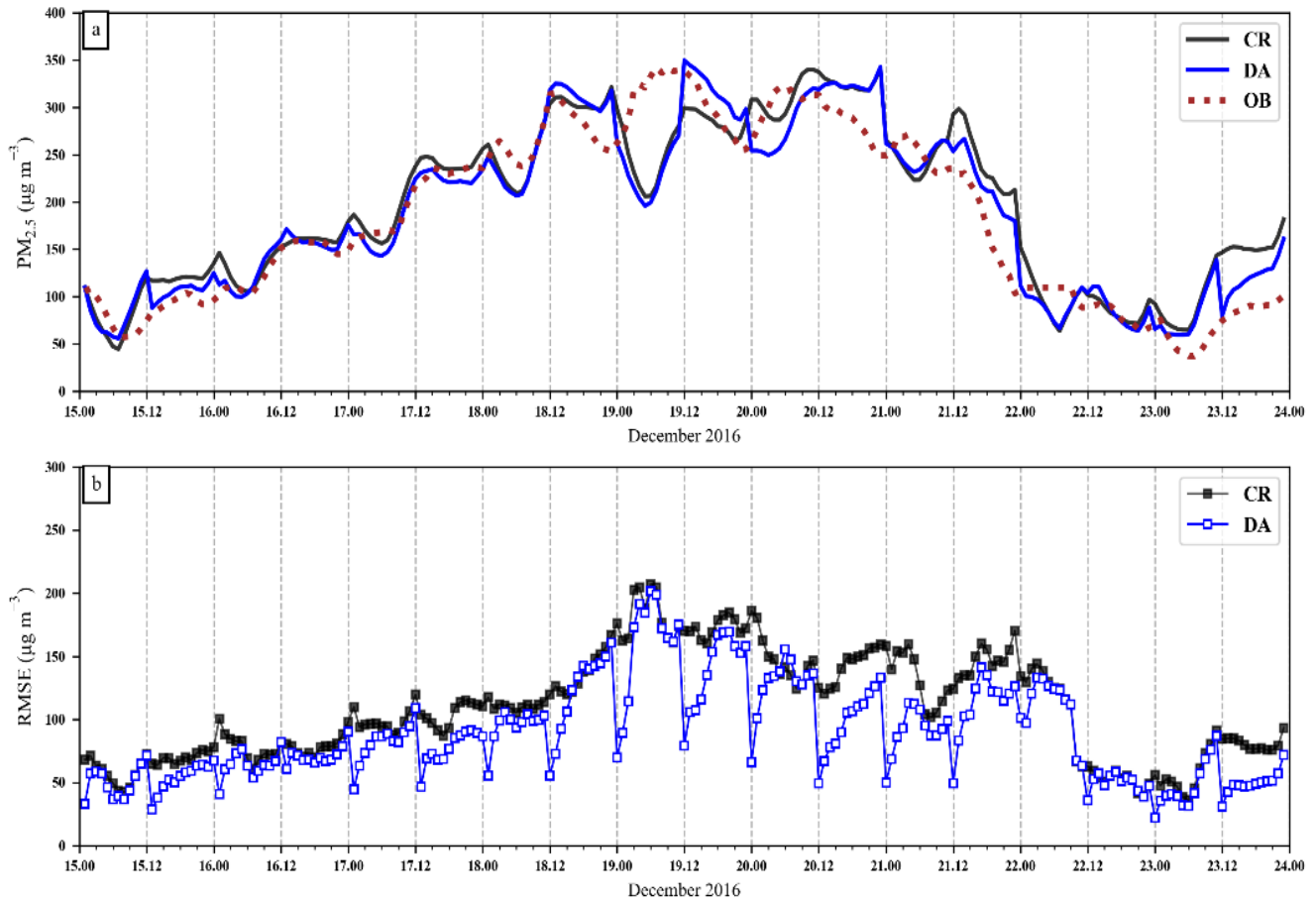


**Figure 8. Rate of improvement (ROI, unit: %) by data assimilation in 1d (24h) predictions for 15 to 23 December 2016 over Mainland China (a), North China (b). The ROI is the ratio of the reduced RMSE statistical metrics to those for the CR simulation. DA00 and DA12 represent the initial field assimilation using EnOI at 0000 UTC and 1200 UTC each day, respectively. DA00 mean and DA12 mean represent the mean ROI over 15 to 23 December 2016 of DA00 and DA12, respectively.**

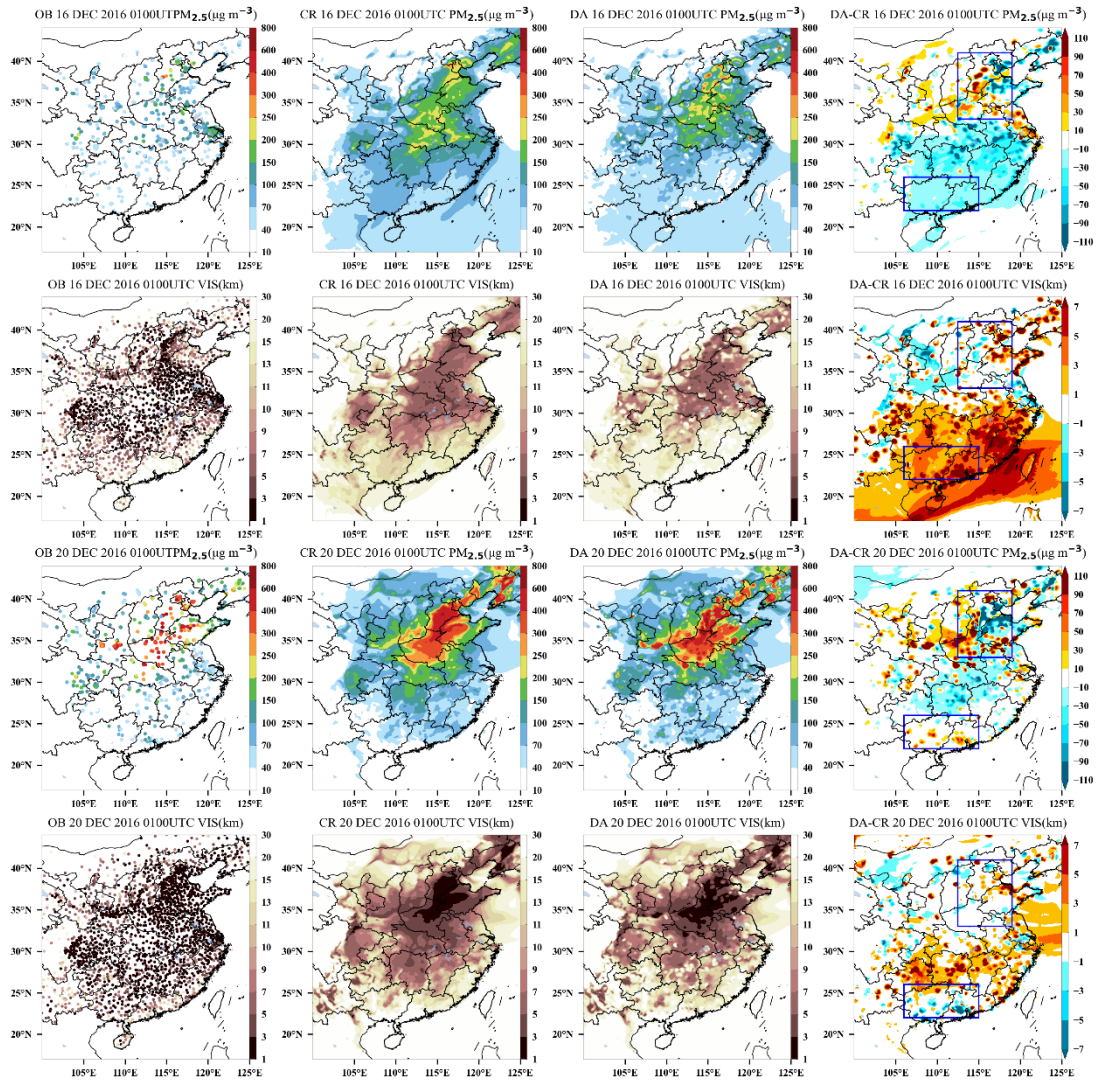
915



920

**Figure 9. Time series of hourly  $PM_{2.5}$  concentration (a) and RMSE between forecasts and observations (b) from 15 December to 23 December 2016 in North China. Red dots: observations, black line: forecasts from control experiment (CR), blue line: forecasts from experiment with initial field assimilation at 0000UTC and 1200UTC (DA), black line with dots: RMSE between CR forecasts and observations, blue line with dots: RMSE between CR forecasts and observations. The values are averages calculated against all the observation sites in North China.**

925



5

Figure 10. Snapshots of PM<sub>2.5</sub> and visibility horizontal distribution for control (CR), assimilation (DA), observation (OB), and increment (DA-CR) at 0100 UTC after assimilation of the initial field at 0000 UTC on 16 and 20 December 2016. The upper box represents northern North China and the lower box represents Guangxi and Hainan in China.

930

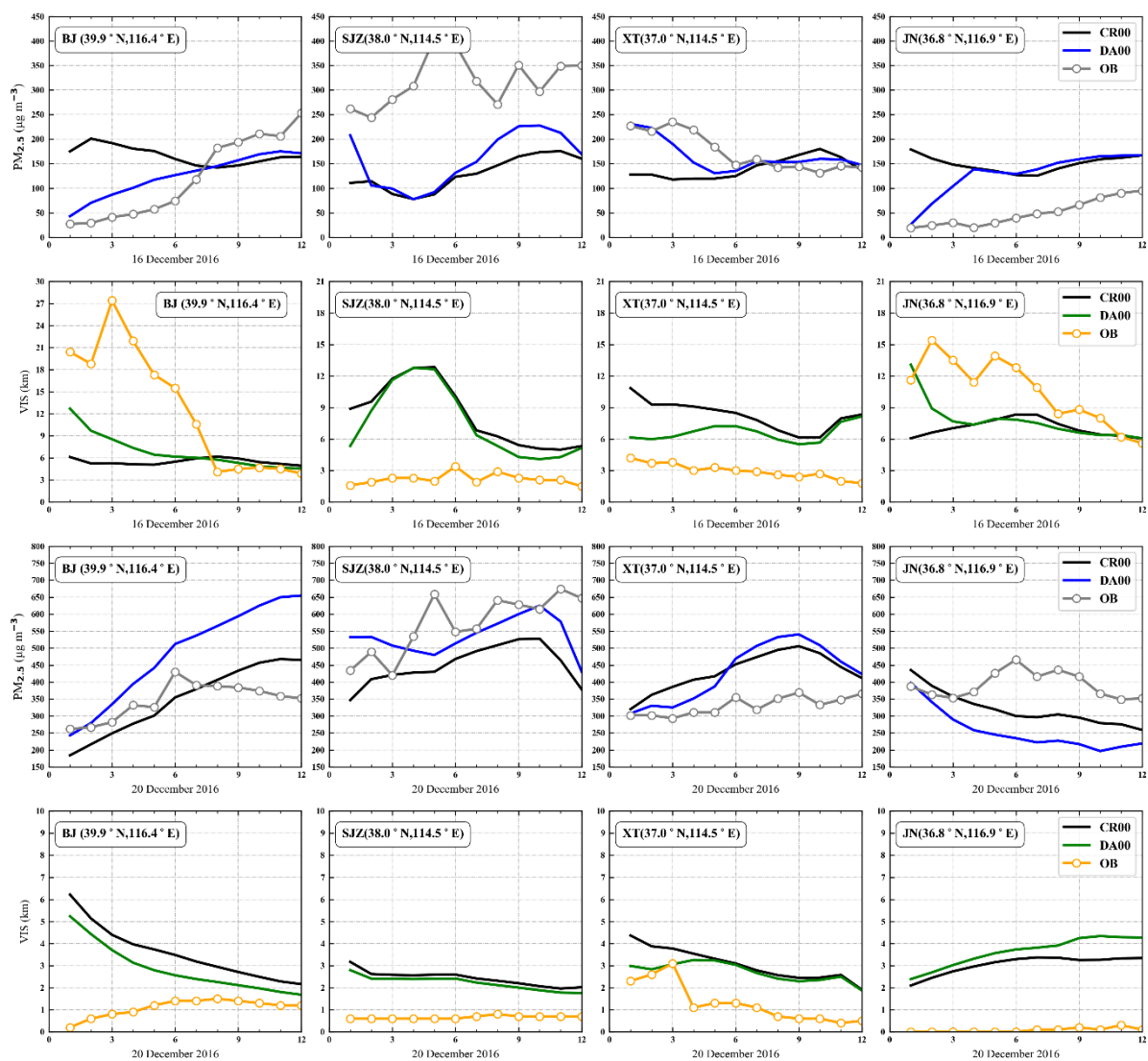


Figure 11. Comparison between of PM<sub>2.5</sub> and visibility observations and model forecast at four cities without (CR00) and with assimilation, assimilation experiment simulations (DA00), and control experiment simulations (CR00) after assimilation (DA00) of the initial field at 0000 UTC on 16 and 20 December 2016 each day. Four cities are exemplified, from left to right, Beijing (BJ), Shijiazhuang (SJZ), Xingtai (XT), Jinan (JN). The labels on the x-axis refer to the first 12 forecast hours of 16 and 20 December 2016 the day, PM<sub>2.5</sub> observations: grey line with circles, visibility observations: orange line with circles, PM<sub>2.5</sub> and visibility model forecast without assimilation: black line, PM<sub>2.5</sub> model forecast with assimilation: blue line, visibility model forecast with assimilation: green line.

935